



School of Biological and Marine Sciences
Faculty of Science and Engineering

2021-02-10

Antagonistic cytoprotective effects of C60 fullerene nanoparticles in simultaneous exposure to benzo[a]pyrene in a molluscan animal model

Awadhesh N. Jha *School of Biological and Marine Sciences*

Let us know how access to this document benefits you

General rights

All content in PEARL is protected by copyright law. Author manuscripts are made available in accordance with publisher policies. Please cite only the published version using the details provided on the item record or document. In the absence of an open licence (e.g. Creative Commons), permissions for further reuse of content should be sought from the publisher or author.

Take down policy

If you believe that this document breaches copyright please [contact the library](#) providing details, and we will remove access to the work immediately and investigate your claim.

Follow this and additional works at: <https://pearl.plymouth.ac.uk/bms-research>

Recommended Citation

Jha, A. N. (2021) 'Antagonistic cytoprotective effects of C60 fullerene nanoparticles in simultaneous exposure to benzo[a]pyrene in a molluscan animal model', *Science of the Total Environment*, 755(1).

Available at: <https://doi.org/10.1016/j.scitotenv.2020.142355>

This Article is brought to you for free and open access by the Faculty of Science and Engineering at PEARL. It has been accepted for inclusion in School of Biological and Marine Sciences by an authorized administrator of PEARL. For more information, please contact openresearch@plymouth.ac.uk.

1 **Antagonistic cytoprotective effects of C₆₀ fullerene nanoparticles in**
2 **simultaneous exposure to benzo[a]pyrene in a molluscan animal**
3 **model.**

4
5 **Michael N. Moore^{*1,2,3}, Susanna Sforzini⁴, Aldo Viarengo⁴, Audrey Barranger^{1,a}, Yann**
6 **Aminot^{1,b}, James W. Readman^{1,3}, Andrei N. Khlobystov^{5,6}, Volker M. Arlt^{7,8,c}, Mohamed**
7 **Banni⁹ and Awadhesh N. Jha¹**

8
9 ¹ School of Biological and Marine Sciences, University of Plymouth, Plymouth PL4 8AA, UK

10 ² European Centre for Environment & Human Health (ECEHH), University of Exeter Medical
11 School, Knowledge Spa, Royal Cornwall Hospital, Cornwall TR1 3LJ, UK

12 ³ Plymouth Marine Laboratory, Prospect Place, The Hoe, Plymouth PL1 3HD, UK

13 ⁴ Institute for the study of Anthropic impacts and Sustainability in marine environment – IAS,
14 National Research Council – CNR, Via de Marini, 6, 16149 Genova GE, Italy

15 ⁵ School of Chemistry, University of Nottingham, University Park, Nottingham NG7 2RD, UK

16 ⁶ Nanoscale and Microscale Research Centre, University of Nottingham, University Park,
17 Nottingham NG7 2RD, UK

18 ⁷ Department of Analytical, Environmental and Forensic Sciences, King's College London,
19 London SE1 9NH, UK Department of Analytical, Environmental and Forensic Sciences,
20 King's College London, MRC-PHE Centre for Environmental & Health, London SE1 9NH,
21 UK

22 ⁸ Toxicology Department, GAB Consulting GmbH, 69126 Heidelberg, Germany

23 ⁹ Laboratory of Biochemistry and Environmental Toxicology, ISA, Chott-Mariem, Sousse,
24 Tunisia

25
26 ^a Present Address: Université de Rennes 1/Centre National de la Recherche Scientifique,
27 UMR 6553 ECOBIO, F-35000 Rennes, France

28 ^b Present Address: Ifremer, RBE/BE/LBCO, Rue de l'Île d'Yeu, BP 21105, Nantes Cedex 3,
29 44311, France

30 ^c Present address: Toxicology Department, GAB Consulting GmbH, 69126 Heidelberg,
31 Germany

32

33

34 * Correspondence: Professor Michael N. Moore; ECEHH, University of Exeter Medical School,
35 Truro, UK; mnm@pml.ac.uk; Tel.: +44-(0)7894-007694

36

37 **Abstract**

38 The hypothesis that C₆₀ fullerene nanoparticles (C₆₀) exerts an antagonistic interactive effect
39 on the toxicity of benzo[a]pyrene (BaP) has been supported by this investigation. Mussels
40 were exposed to BaP (5, 50 & 100 µg/L) and C₆₀ (C₆₀ - 1 mg/L) separately and in combination.
41 Both BaP and C₆₀ were shown to co-localise in the secondary lysosomes of the
42 hepatopancreatic digestive cells in the digestive gland where they reduced lysosomal
43 membrane stability (LMS) or increased membrane permeability, while BaP also induced
44 increased lysosomal lipid and lipofuscin, indicative of oxidative cell injury and autophagic
45 dysfunction. Combinations of BaP and C₆₀ showed antagonistic effects for lysosomal stability,
46 mTORC1 (mechanistic target of rapamycin complex 1) inhibition and intralysosomal lipid (5 &
47 50 µg/L BaP). The biomarker data (i.e., LMS, lysosomal lipidosis and lipofuscin accumulation;
48 lysosomal/cell volume and dephosphorylation of mTORC1) were further analysed using
49 multivariate statistics. Principal component and cluster analysis clearly indicated that BaP on
50 its own was more injurious than in combination with C₆₀. Use of a network model that
51 integrated the biomarker data for the cell pathphysiological processes, indicated that there
52 were significant antagonistic interactions in network complexity (% connectance) at all BaP
53 concentrations for the combined treatments. Loss of lysosomal membrane stability probably
54 causes the release of intralysosomal iron and hydrolases into the cytosol, where iron can
55 generate harmful reactive oxygen species (ROS). It was inferred that this adverse oxidative
56 reaction induced by BaP was ameliorated in the combination treatments by the ROS
57 scavenging property of intralysosomal C₆₀, thus limiting the injury to the lysosomal membrane;
58 and reducing the oxidative damage in the cytosol and to the nuclear DNA. The ROS
59 scavenging by C₆₀, in combination with enhanced autophagic turnover of damaged cell
60 constituents, appeared to have a cytoprotective effect against the toxic reaction to BaP in the
61 combined treatments.

62 **Key words:** antagonism, autophagy, complexity, lysosomes, C₆₀-nanoparticles, oxidative-
63 injury

64 **Introduction**

65 Manufactured nanomaterials (MNMs) including nanoparticles (NPs), nanotubes and
66 nanofibres are increasingly used in a burgeoning growth of industrial and domestic
67 applications (Giese et al., 2018). These materials can enter the natural environment via the
68 atmosphere and waterborne waste (Freixa et al., 2018; Giese et al., 2018). There is only
69 limited data available, however, for how these materials will interact with conventional
70 chemical contaminants, such as the ubiquitous contaminant polycyclic aromatic hydrocarbons
71 (PAHs); and whether such interactions can influence the toxicity of either the NPs or the PAHs
72 themselves (Al-Subiai, et al., 2012; Barranger et al., 2019a, b; Canesi et al., 2014; Della Torre
73 et al., 2018; Freixa et al., 2018; González-Soto et al., 2019; Lee et al., 2011; Sforzini et al.,
74 2018, 2020). Previous investigations have indicated that carbon nanomaterials can exert
75 antagonistic interactive effects on the toxicity and ecotoxicity of organic chemical pollutants
76 (Barranger et al., 2019a, b; Freixa et al., 2018).

77
78 Accumulating evidence on the toxicity of nanoparticles (NPs) indicates that reactive oxygen
79 species (ROS) mediated oxidative cell injury is a generic reaction (Barranger et al., 2019a, b;
80 D'Agata et al., 2014; Dodd and Jha, 2009; Reeves et al., 2008; Sforzini et al., 2020; Stern et
81 al., 2012; Stone & Donaldson, 2006); although, as yet our understanding of the impact of the
82 products of nanotechnology on animal and ecosystem health is still rather limited (Canesi et
83 al., 2014; D'Agata et al., 2014; Della Torre et al., 2018). Animal cells are evolutionarily pre-
84 adapted to internalise nanomaterials by endocytosis or cell feeding (Stern et al., 2012).
85 Hence, most cellular uptake of NPs will probably occur via this route. Fundamental questions,
86 however, remain unanswered as to the significance of engineered NPs on the health of aquatic
87 organisms, as well as interactions between NPs and conventional chemical pollutants, such
88 as ubiquitous organic xenobiotics (e.g., PAHs and nitrogen and sulphur containing
89 heterocyclics). Of concern also are the higher level consequences for damage to animal
90 health, associated ecological risk and the possible food chain risks for humans.

91

92 The lysosomal vacuolar system in the cells of the molluscan digestive gland (hepatopancreas
93 or midgut gland) readily accumulates many harmful environmental contaminants, including
94 metal ions, organic xenobiotics, nano- and micro-plastics and other nanomaterials (Barranger
95 et al., 2019a, b; Jimeno-Romero et al., 2016; Koehler et al., 2008, Lee & Hong, 2020; Moore
96 et al.2004; Sforzini et al., 2018, 2020, Shaw et al., 2019; Von Moos et al., 2012). Lysosomal
97 overload due to sequestration and accumulation of non-degradable foreign materials (e.g.,
98 nanomaterials) and xenobiotic chemicals (e.g., metal ions and organic chemical
99 contaminants) can lead to lysosomal and autophagic dysfunction, involving permeabilisation
100 of the lysosomal membrane and in severe cases release of lysosomal enzymes and cell death
101 (De Duve et al., 1974; Moore et al., 2006, 2007, 2009, Sforzini et al, 2018, 2020; Shaw et al.,
102 2019; Stern et al., 2012). Furthermore, continuous digestion within lysosomes of iron-
103 containing metallo-proteins, from both endocytosed food and autophagy of cell constituents,
104 produces a pool of labile, redox-active, low-molecular-weight iron, which may make these
105 organelles particularly susceptible to oxidative damage (Kurz et al., 2008; Lowe & Moore,
106 1979; Yu et al., 2003). Oxidant-mediated destabilization of lysosomal membranes with release
107 of iron and hydrolytic enzymes into the cytoplasm can lead to an oxidative and hydrolase-
108 mediated cascade of degradative and injurious events resulting in cell death (Kirchin et al.,
109 1992; Stern et al., 2012; Winston et al., 1991; Yu et al., 2003).

110

111 C₆₀ fullerene has been reported to induce autophagy in various cells, including molluscan
112 digestive cells using lysosomal membrane destabilisation, lysosomal volume increase and
113 LC3 (microtubule-associated proteins 1A/1B light chain 3B) as the biomarkers (Sforzini et al.,
114 2020; Stern et al., 2012). The autophagic reaction to the nanoparticles is probably mediated
115 by oxidative inhibition (i.e., dephosphorylation) of mTORC1 (mechanistic target of rapamycin
116 complex 1) by an elevated flux of ROS generated as a result of intra-lysosomal iron release
117 into the cytosol, as a result of lysosomal membrane destabilisation (i.e., permeabilisation) as

118 mentioned above (Brunk & Terman, 2002; Sforzini et al., 2020; Stern et al., 2012; Yu et al.,
119 2003).

120

121 C₆₀ fullerene has the ability to both scavenge and generate (i.e., light-activated) ROS due to
122 its physico-chemical properties (Halenova et al., 2018; Lee et al., 2011). The feature that
123 mediates most of the fullerene's biological and toxic interactions is its particular sensitivity to
124 the covalent attachment of functional groups to the fullerene core, as well as to the physico-
125 chemical changes introduced by solubilisation procedures for the preparation of fullerene
126 nanoparticles (Markovic & Trajkovic, 2008).

127

128 Barranger et al. (2019a, b) have previously described antagonistic effects on DNA damage in
129 mussels for the interactions between benzo[a]pyrene (BaP) and C₆₀ fullerene (C₆₀) and multi-
130 walled carbon nanotubes (MWCNTs). Adverse cell pathological effects of BaP and C₆₀
131 individually on DNA damage and sub-cellular injury have also been described from previous
132 investigations (Al-Subiai et al., 2012; Barranger et al., 2019a; González-Soto et al., 2019;
133 Sforzini et al., 2018, 2020).

134

135 Consequently, the aim of this investigation was to examine the possible interactive effects of
136 simultaneous exposure to BaP and C₆₀ on marine mussels, an ecologically important bio-
137 indicator and ecological foundation species. The hypothesis was tested that C₆₀ fullerene
138 exerts a cytoprotective antagonistic interactive effect on the toxicity of BaP (Barranger et al.,
139 2019a, b; Freixa et al., 2018; Lee et al., 2011). Additionally, we also wanted to investigate
140 whether there was any further evidence for either an antagonistic or synergistic ("Trojan
141 Horse") effect between the polycyclic aromatic hydrocarbon BaP and the C₆₀ nanoparticles.
142 Chemical analyses of the digestive gland tissue, as well as molecular and sub-cellular
143 biological reactions or biomarkers (viz., DNA damage – Comet assay, LMS, lysosomal
144 lipidosis, lysosomal lipofuscinosis, lysosome/cell – L/C volume as an autophagy biomarker,
145 and phosphorylated mTORC1) were used examine the effects of BaP and C₆₀ on tissue

146 uptake, lysosomal function, induced autophagic cellular reactions, and oxidative cell injury.
147 Principal component analysis (PCA) and cluster analysis, together with interactive network or
148 complexity modelling was used to integrate multi-biomarker data into a mechanistic
149 explanatory framework; and to test the predictive capability of a previously developed network
150 complexity model of cellular patho-physiological function for DNA damage (Comet assay) and
151 programmed cell death (PCD) in molluscan digestive cells (Banni et al., 2017; Barranger et
152 al., 2019a, b; Lowe, 1988; Sforzini et al., 2018). Network complexity and statistical modelling
153 were also deployed in order to facilitate the integration of the biomarker findings and to
154 facilitate their interpretation in a mechanistic context, as was previously implemented with
155 separate BaP and C₆₀ fullerene treatments (Sforzini et al., 2018, 2020).

156

157 **Materials and Methods**

158 *Animal Collection and Husbandry*

159 Mussels (*Mytilus galloprovincialis*; 45–50 mm) were collected from the intertidal zone at
160 Trebarwith Strand, Cornwall, UK (50° 38' 40" N, 4° 45' 44" W) in October 2016. This site has
161 previously been used as a reference location for ecotoxicological studies and is considered
162 relatively clean with a minimum presence of disease (Bignell et al., 2011; Shaw et al., 2011).
163 Following collection, mussels were transported to the laboratory in cool boxes and placed in
164 an aerated tank at a ratio of 1 mussel /L with natural seawater from Plymouth Sound (filtered
165 at 10 µm). Mussels were maintained at 15°C, fed with micro-algae (*Isochrysis galbana* -
166 Interpret, UK) every 2 days with a 100% water change 2 h post feeding.

167

168 *Preparation of Stock Solutions*

169 Fullerenes (C₆₀)

170 C₆₀ stock solutions were prepared as described by Barranger (2019a). C₆₀ was obtained from
171 Sigma Aldrich (Gillingham, UK) and Designer Carbon Materials Ltd. (Oxford, UK),
172 respectively. In order to better replicate the conditions of the experiment during analysis, 2
173 mussels were maintained in 2 L glass beakers for 24 h with natural seawater from Plymouth

174 Sound (filtered at 10 µm). Subsequently, fullerenes (1 mg) were added to the mussel-exposed
175 seawater (10 mL) and the suspension homogenised by ultrasonication (Langford Sonomatic
176 375, Bromsgrove, UK, 40 kHz) for 1 h at room temperature. The suspension was allowed to
177 settle for at least 4 h at room temperature prior to analysis of the aggregate size. Dynamic
178 light scattering (DLS) was performed using a Malvern Zetasizer Nano-ZS (Malvern, UK) at
179 room temperature; and the results obtained were the average of 3 measurements (Barranger
180 et al., 2019a). Bright field transmission electron microscopy (TEM) and dark-field scanning
181 transmission electron microscopy (STEM) were performed using a JOEL 2100+ microscope
182 (Welwyn Garden City, UK) operated at 200 keV. Energy dispersive X-ray (EDX) spectra were
183 acquired using an Oxford Instruments INCA X-ray microanalysis system (Oxford, UK) and
184 processed using Aztec software (version 3.1 SP1, Oxford, UK). Samples were prepared by
185 casting several drops of the respective suspensions onto copper grid-mounted lacy carbon
186 films.

187

188 The C₆₀ concentrations used in this study were based on previous experiments in our
189 laboratory using marine mussels (Al-Subiai et al., 2012; Barranger et al., 2019a; Di et al.,
190 2017; Moore et al., 2009; Sforzini et al., 2020).

191

192 Benzo[a]pyrene (BaP)

193 BaP (≥ 96%, B1760, Sigma Aldrich) was dissolved in dimethyl sulfoxide (DMSO) and aqueous
194 solutions were prepared so that the DMSO concentration in the sea water was 0.001%
195 (Barranger et al., 2019a). The BaP concentrations used in this study were based on previous
196 experiments in our laboratory using marine mussels (Al-Subiai et al., 2012; Di et al., 2011,
197 2017).

198

199 *Experimental design, exposure of animals to BaP and C₆₀ and sampling*

200 Experimental design has been described in detail by Barranger et al. (2019a). Following
201 depuration, mussels were separated (2 mussels per beaker) into 2 L glass beakers containing

202 1.8 L of seawater and allowed to acclimate for 48 h. A photoperiod of 12 h light: 12 h dark was
203 maintained throughout the experiment. Seawater was aerated (i.e., aquarium pumps and
204 airstones) and monitored in each of the beakers by measuring salinity with a digital salinity
205 meter ($36.45 \pm 0.19\%$). Mussels (26 mussels with 2 mussels per 2L beaker for each treatment)
206 were exposed for 3 days with no water changes to the solvent control, BaP (5, 50 and 100
207 $\mu\text{g/L}$), C₆₀ alone (1 mg/L) and a combination of BaP (5, 50 and 100 $\mu\text{g/L}$) and C₆₀ (1 mg/L).
208 Control groups received only DMSO at the same concentrations as used in the other exposure
209 groups (i.e., 0.001% DMSO). After 3-day treatment period, mussel sex was determined by
210 mantle smear and light microscopy. Digestive glands from 10 female animals were rapidly
211 removed, placed on aluminium cryostat chucks, chilled in super-cooled n-hexane and stored
212 at -80°C for cytochemistry and immunocytochemistry (Sforzini et al., 2018). Digestive glands
213 from female mussels were subsequently processed for immunocytochemical and
214 cytochemical analysis (Sforzini et al., 2018).

215
216 Following exposure, digestive gland (DG) tissue was collected from 9 mussels for each
217 treatment for BaP and C₆₀ analyses, washed in toluene and pooled (3 mussels per tissue
218 replicate and then extracted with toluene.

219
220 *Analyses of benzo[a]pyrene and C₆₀ fullerene in digestive gland tissue*

221 The analyses of BaP and C₆₀ were performed on the toluene extracts. Tissue extracts were
222 analysed for BaP using an Agilent Technologies (Stockport, UK) 7890A Gas Chromatography
223 (GC) system interfaced with an Agilent 5975 series Mass Selective (MS) detector as described
224 by Banni et al. (2017). The tissue extracts were analysed for C₆₀ using ultrahigh performance
225 liquid chromatography coupled with high resolution mass spectrometry following a protocol
226 adapted from Sanchís et al. (2019).

227
228 *Cytochemical analyses*

229 Frozen digestive gland sections (10 µm) of mussels from each exposure condition were cut
230 using a cryostat microtome (Leica CM3050) and flash-dried by transferring them onto poly-L-
231 lysine-coated microscope slides at room temperature.

232

233 Lysosomal membrane stability (LMS)

234 The determination of LMS in the cells of the digestive gland was performed on cryostat tissue
235 sections following essentially the method described by Moore (1988) and Moore et al. (2008).
236 This cytochemical assay is based on acid labilization characteristics of latent hydrolase β -N-
237 acetylhexosaminidase (NAH) using naphthol-AS-BI-N-acetyl- β -D-glucosaminide as a
238 substrate for NAH, and diazonium post-coupled with fast violet B. Slides were observed using
239 an inverted microscope (Zeiss Axiovert 100M) at 400 x magnification, connected to a digital
240 camera (Zeiss AxioCam). The pictures obtained were analysed using an image analysis
241 system (Scion Image) that allowed for the determination of the labilisation period i.e. the
242 incubation time in the acid buffer needed to produce the maximal lysosomal staining.

243

244 Lysosomal/cytoplasmic (L/C) volume ratio

245 The L/C volume ratio of the digestive gland tissue was evaluated following the method
246 described by Moore (1976) and Moore and Clarke (1982). Lysosomes were reacted for the
247 lysosomal enzyme β -N-acetylhexosaminidase (NAH) using naphthol-AS-BI-N-acetyl- β -D-
248 glucosaminide as a substrate for NAH as for LMS above. The ratio between cytoplasmic and
249 lysosomal volumes was determined by analysing the images obtained from the slides at 400
250 x magnification by image analysis as described above and expressed as a percentage
251 variation with respect to controls.

252

253 Lysosomal lipidoses and lipofuscin accumulation

254 Lysosomal accumulation of triglyceride lipids (neutral lipids) or lipidoses was determined using
255 the Oil Red O method (Moore et al., 2008). Lipofuscin accumulation (lipofuscinosis) in
256 lysosomes was determined *via* the Schmorl assay as previously described (Moore, 1988;

257 Moore et al., 2008). Lipofuscin and lysosomal lipidosis were assessed using image analysis
258 to determine relative absorbance of their respective cytochemical reaction product (Moore
259 1988; Moore et al., 2008; Sforzini et al., 2020).

260

261 *Immunocytochemical analyses*

262 Immunofluorescence for BaP, C₆₀ fullerene and lysosomal cathepsin D

263 Frozen digestive gland sections (10 µm) of mussels from each exposure condition were cut
264 using a cryostat microtome (Leica CM3050) and flash-dried by transferring them onto poly-L-
265 lysine-coated microscope slides at room temperature. Sections were then fixed in
266 paraformaldehyde (PFA) solution (4% PFA in phosphate buffer saline-PBS, pH 7.2, 20 min at
267 20 ± 1 °C).

268

269 Immunofluorescent anti-PAHs and anti-C₆₀ staining has been described in detail by Sforzini et
270 al. (2018, 2020). To study the possible accumulation of BaP and C₆₀ in the lysosomes of the
271 digestive gland cells of exposed mussels, immunofluorescence co-localization of BaP, C₆₀ and
272 the lysosomal enzyme cathepsin D was performed following the method described in Sforzini
273 et al. (2018, 2020).

274

275 Colocalization of C₆₀ and BaP by double immunolabelling with monoclonal antibodies from the
276 same species was performed as described by Eichmüller et al. (1996), with slight
277 modifications. Digestive gland tissue sections were reacted with the anti-fullerene (anti-C₆₀)
278 antibody, as reported above for the single labelling (Sforzini et al., 2020). The anti-PAH
279 antibody (monoclonal mouse, Santa Cruz Biotechnology Inc., 1/100 in PBS containing 1%
280 BSA), used to detect BaP, was coupled *in vitro* to the secondary antibody (goat polyclonal to
281 mouse Alexa Fluor® 568, 1/50, 1h, 37°C; Sforzini et al., 2014, 2018). Normal mouse serum
282 (0.5%) was then added to saturate excess free anti-mouse binding sites on the secondary
283 antibody (1h at 37°C). Before applying the antibodies-complex solution, sections were

284 incubated with the mouse serum IgG₁ (0.5%, 2% BSA, in PBS, 1h, 20±1°C). Following the
285 immune-reaction with the antibodies-complex (2h, 20±1°C), sections were rinsed in PBS,
286 stained with DAPI and then mounted in Mowiol mounting medium (Cold Spring Harbour
287 Protocols, 2006; <http://cshprotocols.cshlp.org/>).

288

289 Immunofluorescence for anti-phosphorylated-mTORC1

290 Tissue sections prepared as described above were incubated in a permeabilisation and
291 blocking solution (0.5% Triton X-100, 2% BSA, 0.5% goat serum in PBS, 1 h at 20 ± 1 °C) and
292 then with the primary antibody (anti m-TOR (phospho S2448) antibody , Abcam, 1/100 in PBS
293 containing 1% BSA and 0.05% Triton X-100) overnight at 4 °C in a moist chamber. Sections
294 were then washed three times in PBS (5 min) and the secondary antibody was applied, i.e.
295 polyclonal goat to rabbit (Chromeo) (Abcam) (1/100 in 1% BSA and 0.05% Triton X-100 in
296 PBS) for 1 h at 20 ± 1 °C in the dark. Finally, sections were rinsed in PBS, counterstained with
297 propidium iodide and mounted. Immunocytochemical controls for non-specific fluorescence
298 included sections that were processed in the absence of the primary or secondary antibodies.
299 Slides were viewed under 400 × magnification by an inverted photo-microscope (Zeiss
300 Axiovert 100M connected to a digital camera Zeiss AxioCam MRm) equipped for fluorescence
301 microscopy using FITC, Rhodamine and DAPI emission filters. Images were analysed using
302 an image analysis system (Scion Image) that allowed for the quantification of the mean
303 fluorescence intensity.

304

305 *Determination of DNA strand breaks using the comet assay*

306 DNA damage (Comet assay) was determined as described in detail by us in earlier
307 publications (Banni et al., 2017; Barranger et al., 2019a,b). Digestive gland tissues were
308 stored on ice prior to processing for the comet assay. After rough chopping, each piece of
309 tissue was added to 1 mL of 1.6 mg/mL dispase II solution (in Hank's buffered saline) pre-
310 warmed to 37°C. After digesting in the dark for 30 min, the resulting suspension was coarsely
311 filtered through gauze and spun at 200 g to remove any debris. The supernatant was checked

312 for cell viability using trypan blue (0.04%), and only samples with >90% unstained cells were
313 used. A sub-sample of 100 μ L of the cell suspension was pelleted at 350 g and 180 μ L low
314 melting point agarose added. Two replicate microgels (75 μ L) were formed by cover-slipping
315 and allowed to set at 4°C for a minimum of 15 min. After the cover slips were removed, cells
316 were lysed in 2.5 M NaCl, 100 mM EDTA, 10 mM Tris, 1% N-laurylsarcosine, 1% Triton X-
317 100, and 10% DMSO (adjusted to pH 10 with NaOH) for 1 h at 4°C in the dark. Slides were
318 then transferred to an electrophoresis chamber containing 1 mM EDTA and 0.3 M NaOH (pH
319 13). DNA was allowed to unwind in the dark for 20 min, followed by electrophoresis at 1 V/cm
320 (~300 mA) for 20 min in the dark. Gels were preserved with ice cold 100% ethanol and then
321 scored after the addition of 20 μ g/mL ethidium bromide using a Leica epifluorescence
322 microscope (Leica Microsystems, Milton Keynes, UK) and Comet 4 image analysis system
323 (Perceptive Instruments, Bury St Edmunds, UK). One hundred nucleoids were assessed per
324 slide; all samples were measured blind. Tail intensity (% tail DNA), defined as the percentage
325 of DNA migrated from the head of the comet into the tail, was used as a measure of DNA
326 damage induced.

327

328 *Programmed cell death (PCD) determination*

329 Digestive tubule atrophy or breakdown was used as a proxy for PCD and was determined
330 from previously described histopathological and cytochemical investigations of mussel
331 digestive cells by Lowe (1988) and Moore (1988) that enabled the derivation of the relationship
332 between LMS and tubule atrophy (inversely correlated: $R^2 = 0.7745$, $R = -0.8801$, $P \leq 0.001$,
333 $n = 40$).

334

335 *Univariate statistical analysis*

336 Five replicates per control and experimental treatment concentration were analysed. Each
337 replicate consisted of the digestive gland from one mussel; the mussels were collected from

338 a separate beaker. The non-parametric Mann-Whitney U-test, and the parametric t-test was
339 used to compare the data from treated mussels with those of the controls.

340

341 *Multivariate statistical analysis*

342 The cellular biomarker data (i.e., LMS, L/C vol., lipid, lipofuscin and phosphorylated mTORC1)
343 for five mussels from each experimental treatment were analysed using non-parametric
344 multivariate analysis software, PRIMER v 6 (PRIMER-C Ltd., University of Auckland,
345 Auckland, New Zealand; Clarke, 1999; Clarke & Warwick, 2001) as previously described by
346 Sforzini et al. (2018, 2020). All data were log transformed [$\log_n(1+x)$] and standardised to the
347 same scale. Correlations between biomarkers were tested using a scatter plot matrix
348 (PRIMER v 6, Draftsman Plot). The multivariate analysis was conducted with and without data
349 for C₆₀ at 0.01 and 0.1 mg/L that was reported previously by Sforzini et al. (2020) in addition
350 to C₆₀ at 1 mg/L, as was used for the mixtures with BaP treatments. Correlations between the
351 various cellular biomarkers and the first and second principal components (PC 1 & PC 2; C₆₀
352 at 1 mg/L only) were also derived

353

354 Finally, in order to map integrated biomarker data onto “health status space” (measured as
355 first principal components – PC 1), PC 1 values were plotted against both the complexity
356 values (system or network complexity - connectance C_v%), and LMS as measures of cellular
357 well-being for each experimental treatment (Sforzini et al., 2018, 2020).

358

359 *Network modelling*

360 Model description

361 The generic cell model described by Moore (2010) has been developed from extensive
362 published data in the environmental toxicology and biomedical literature, and the large-scale
363 organisation of metabolic networks (Cuervo, 2004; Di Giulio & Hinton, 2008; Jeong et al.,
364 2000; Juste & Cuervo, 2019; Levine, 2005; Moore, 2020). This cellular interaction network
365 was constructed around the essential processes of feeding, excretion and energy metabolism

366 (Fig 1A). Protein synthesis and degradation, including lysosomal autophagy, and fusion of
367 secondary lysosomes with other secondary lysosomes are also incorporated in the model as
368 are the major protective systems (Livingstone et al., 2000; Moore, 2010; Sforzini et al., 2018).
369 A modified subset of the generic model incorporating oxidative cell injury was used in this
370 investigation in order to accommodate the available data (Fig. 1B). The directed cellular
371 physiological networks were constructed using *Cytoscape 3.3.0* software (Shannon et al.,
372 2003).

373

374 Analysis of cell system complexity

375 Whole system complexity in the directed cellular physiological network was evaluated using
376 connectedness (Bonchev, 2003). Topological complexity was measured as connectedness or
377 connectance (C_v %) is the ratio between the number of links E in the interaction network and
378 the number of links (edges) in the complete graph having the same number of nodes or
379 vertices (V) (Bonchev, 2003). Connectedness relates the number of nodes (vertices) V and
380 links or edges (arcs in a directed link) E where the connectance percentage ratio, $C_v\%$, of a
381 directed graph (digraph) with V nodes or vertices is then:

382

$$383 \quad C_v \% = [1 / \max (C_v)] \lceil E \rceil \times 100 \quad (\text{Equation 1})$$

384

385 which reduces to:

386

$$387 \quad C_v \% = (\lceil E \rceil / V^2) \times 100 \quad (\text{Equation 2})$$

388

389 as shown in Equations 1 & 2 for typical digraphs that allow every node to connect to every
390 other node, where $\lceil E \rceil$ is the nearest integer function of E (Davis, 1997). This method uses
391 the sum of the edge weights rather than the edge count and allows for self-loops or arcs (Fig.
392 1A & B). The network also contained a node for DNA damage although this data was not

393 included in the calculation of connectance. DNA damage (Comet assay) had been determined
394 previously in animals from the same experiment (Barranger et al., 2019a).

395

396 Transformed biomarker data were used to attribute proportional weight values to the
397 interactions (edges) between cellular physiological processes (nodes) as previously described
398 (Sforzini et al., 2018; Fig. 1B). The various biomarker values were standardised to a proportion
399 of Control mean values. These values (x) were then used for biomarkers that normally
400 decrease with pathology (i.e., lysosomal membrane stability & mTORC1), while biomarkers
401 that normally increase with pathology (i.e., lysosomal lipid, lysosomal/cell volume ratio &
402 lipofuscin) were further transformed to their reciprocal value (x^{-1}). All standardised and
403 transformed values were normalised using \log_{10} transformation of x or x^{-1} as appropriate; and
404 then inputted into the model as the weight values for the network interaction strengths (edge
405 or link strength). Finally, the non-parametric Mann-Whitney U-test, and the parametric t-test
406 was applied to the connectance ($C_v\%$) values of the control and experimental treatment groups
407 to test for statistical differences. Network or system complexity was plotted against PC 1, LMS,
408 DNA damage (Comet assay for DNA strand breaks) and predicted PCD.

409

410 *Analysis of interactions using Interaction Factor (IF)*

411 Analysis of the combined effects of C₆₀ and BaP on the biomarkers (i.e., lysosomal membrane
412 stability, mTORC1, lysosomal lipid, lipofuscin & lysosomal/cytoplasmic volume ratio) was
413 performed by calculating the Interaction Factor (IF) in order to test for evidence of additivity,
414 synergism and antagonism as shown in Equations 3-5 (Barranger et al., 2019a, b; David et
415 al., 2016; Katsifis et al., 1996; Schlesinger et al., 1992; Zhang et al., 2019):

416

$$417 \quad \mathbf{IF = (G_{(C60 + BaP)} - C) - [(G_{(C60)} - C) + (G_{(BaP)} - C)]} \quad (\text{Equation 3})$$

418

$$419 \quad \mathbf{= G_{(C60 + BaP)} - G_{(C60)} - G_{(BaP)} + C} \quad (\text{Equation 4})$$

420

421
$$SEM_{(IF)} = \sqrt{(SEM^2_{(C60 + BaP)} + SEM^2_{(C60)} + SEM^2_{(BaP)} + SEM^2_{(C)})}$$
 (Equation 5)

422

423 Where IF is the interaction factor: negative IF denotes antagonism, positive IF denotes
 424 synergism, and zero IF denotes additivity. G is the mean cell pathological reaction to toxicants
 425 (BaP, C₆₀ and BaP + C₆₀), C is the mean cellular response under control conditions. For
 426 lysosomal membrane stability (LMS) and the phosphorylated mTORC1, the IF value was
 427 negatively transformed [-1(IF)] because the experimental treatment generally results in a
 428 decrease in the biomarker value compared to the control rather than an increase, which is
 429 standard for the IF test. SEM(x) is the standard error of the mean for group X. Results were
 430 expressed as IF, and the 95% confidence limits were derived from the combined SEM values.

431

432 In order to test the mixture IF values against predicted additive values (assumed to have an
 433 IF = 0), the additive mean values (A) were calculated as shown in Equation 6:

434

435
$$A = (G_{(C60)} - C) + (G_{(BaP)} - C)$$
 (Equation 6)

436

437 The Pythagorean theorem method for combining standard errors was used to derive combined
 438 standard errors for the predicted mean additive values (A) of C₆₀ and BaP
 439 ([http://mathbench.org.au/statistical-tests/testing-differences-with-the-t-test/6-combining-sds-
 440 for-fun-and-profit/](http://mathbench.org.au/statistical-tests/testing-differences-with-the-t-test/6-combining-sds-for-fun-and-profit/)). The standard errors (SEM) for the three C₆₀ and BaP treatments (predicted
 441 additive) were derived using the following Equation 7:

442

443
$$SEM_{(add)} = \sqrt{(SEM^2_{(C60)} + SEM^2_{(BaP)} + SEM^2_{(C)})}$$
 (Equation 7)

444

445 This enabled the 95% confidence limits to be derived for the predicted additive values. The
 446 confidence limits (95% CL/ $\sqrt{2}$) were used to test the predicted additive values having an IF =
 447 0 against the IF values for the mixtures (Buzatto et al., 2015; Lowe et al., 1981).

448

449 **Results**

450 *Analyses of digestive gland for C₆₀ and BaP*

451 The results for the chemical analyses of tissues have been previously reported by Barranger
452 et al. (2019a). Both C₆₀ fullerene and BaP accumulated in the tissues of the digestive gland
453 (Fig. 2A & B). In our study, we analysed for the first time in a marine bivalve, BaP uptake (at
454 different exposure concentrations) in the digestive gland in the presence of C₆₀ fullerene in
455 order to highlight a possible role of contaminant carrier of C₆₀. Comparable BaP tissue
456 concentrations in the presence or absence of C₆₀ were observed (Fig. 2A).

457

458 Low but quantifiable amounts of C₆₀ in digestive gland tissues indicated active uptake, with
459 adsorption on the outside of the tissue ruled out due to external washes with toluene prior to
460 analysis (Fig. 2). High variability in C₆₀ concentrations in the digestive gland makes it difficult
461 to detect a difference between treatments in accumulation of C₆₀ by mussels.

462

463 *Biomarker evaluation and cellular localisation of C₆₀ fullerene and benzo[a]pyrene*

464 All the different treatments utilised in this study induced adverse cellular reactions (i.e.
465 mTORC1, lysosome/cell volume ratio (L/C volume ratio), lysosomal lipofuscin, lysosomal lipid
466 and DNA damage) in the digestive gland of mussels, without affecting their survival (data not
467 shown) during the time course of the experimental treatments. Representative images for the
468 cellular changes in mTORC1, lysosome/cell volume ratio (L/C vol.; autophagy biomarker),
469 lipofuscin and lysosomal lipidosis (triglyceride) are shown in Figure 3A-D. Additionally, Figure
470 4A-D showed that the BaP and C₆₀ were both co-localised in the digestive cell secondary
471 lysosomes, using cathepsin-D as an immunocytochemical marker for lysosomes.

472

473 As shown in Fig. 5 (A - E), all the biomarkers that were strongly related to the autophagic
474 process (i.e. LMS, phosphorylated mTORC1 and L/C volume ratio) showed a similar trend in
475 mussels exposed to BaP (5, 50, 100 µg/L), C₆₀ (1 mg/L), and also in the combined treatments
476 (MIX). In particular, there was a decrease in LMS, and mTORC1 phosphorylation compared

477 to controls. The evaluation of L/C volume ratio showed significant increases in this biomarker
478 in the treated animals, with the exception of the lowest BaP concentration (5 µg/L).

479

480 The results for lysosomal lipofuscin content (an oxidative injury biomarker) showed that BaP
481 caused a significant increase of this parameter at all the concentrations tested, with a
482 maximum at 100 µg/L with respect to controls (Fig. 5D). Otherwise, no significant change was
483 observed in C₆₀ exposed mussels; while the combined treatments (MIX) showed a similar
484 trend to that of BaP, but for 5 and 50 µg/L BaP with lower values, while the mixture at 100 BaP
485 was not significantly different from the control (Fig. 5D). The evaluation of lysosomal lipid
486 (triglyceride) accumulation (biomarker revealing an alteration of lipid metabolism) showed that
487 in mussels exposed to BaP there was a significant increase of lipid content, with a maximum
488 at 50 µg/L (Fig. 5E). No significant increase was found in C₆₀ as well in combined treatment
489 (MIX) of 1.0 mg/L C₆₀ and 5 µg/L BaP exposed animals; similar changes to those observed in
490 BaP treatments were induced in animals exposed to the higher MIX concentrations.

491

492 Pairwise statistical testing between the BaP and combined (MIX) treatments showed that there
493 were significant decreases ($P \leq 0.05$, Mann-Whitney U-test, t-test) in the combined treatments
494 for LMS (MIX 5, 50 & 100 µg/L BaP), mTORC1 (MIX 5, 50 & 100 µg/L BaP), lysosomal lipid
495 (MIX 5 & 50 µg/L BaP), lysosomal lipofuscin (MIX 100 µg/L BaP) and network complexity (MIX
496 5 & 50 µg/L BaP) compared with the corresponding BaP treatments (Fig. 5A, B, D, E). The
497 autophagy biomarker (L/C volume ratio), however, showed a significant increase ($P \leq 0.05$,
498 Mann-Whitney U-test, t-test) in the combined treatment (MIX 5 µg/L BaP) compared with the
499 corresponding BaP treatment (Fig. 5C).

500

501 *Multivariate analysis of biomarker reactions*

502 PCA and hierarchical cluster analysis of all the biomarker reactions showed that all
503 experimental treatments compared to the control, had a detrimental effect on the patho-

504 physiology of digestive cells in mussels (ANOSIM, $P \leq 0.01$; Fig. 6). The first principal
505 component (PC 1) represented 52.5% of the variability and is significantly correlated with all
506 five biomarkers (Table 1). However, the second principal component (PC 2), which
507 represented 24.6% of the variance, was strongly correlated with lipofuscin and lysosomal lipid
508 (Table 2), which corresponded to the BaP treatments. Analysis of similarity shows that C_{60}
509 and BaP 100 $\mu\text{g/L}$ were significantly different ($P \leq 0.05$), and that BaP at all three
510 concentrations were significantly different from their corresponding mixtures (ANOSIM, $P \leq$
511 0.01), and C_{60} and the mixture ($C_{60} + \text{BaP } 100 \mu\text{g/L}$) were significantly different ($P < 0.05$).
512 Overall analysis of similarity showed a highly significant value for dissimilarity (ANOSIM,
513 Global R Statistic: $R = 0.567$, $P \leq 0.001$). Regression analysis (Scatter Plot matrix excluding
514 0.01 and 0.1 mg/L C_{60}) of the biomarker data indicated that many of the biological parameters
515 were significantly correlated, particularly those directly related to autophagy: - LMS, L/C
516 volume and dephosphorylation of phosphorylated mTORC1 (Fig. 7).

517

518 *Network modelling biomarker reactions to $C_{60} + \text{BaP}$ treatments*

519 Inputting the biomarker data into a directed cellular interaction network (digraph) model (Fig.
520 1B; Table 2) enabled the determination of the system complexity. Complexity values
521 determined as percentage connectance ($C_v\%$) for the experimental treatments are shown in
522 Figure 5F. There was a significant loss in connectance in all experimental treatments
523 compared with the control ($P \leq 0.005$, Mann-Whitney U-test, t-test). Pairwise statistical testing
524 between the BaP and combined (MIX) treatments showed that there were significant
525 decreases ($P \leq 0.05$, t-test) in the combined treatments for network complexity measured as
526 connectance (MIX 5 & 50 $\mu\text{g/L}$ BaP) compared with the corresponding BaP treatments (Fig.
527 5F).

528

529 The connectance analysis of these biomarkers data demonstrated that in mussels exposed to
530 all treatments there was a loss of functional complexity (cellular homeostasis), with respect to

531 controls; the maximum loss of connectance was found in animals exposed to 100 µg/L BaP
532 (Fig. 5F).

533

534 The determination of node degree indicated that lysosomal function, autophagy and oxidative
535 cell injury were the most highly connected nodes (vertices) with 7 degrees (number of links or
536 edges), making them important patho-physiological hubs (Fig. 1B). In the more
537 comprehensive network shown in Figure 1A, lysosomal function and autophagic function were
538 the most connected nodes, underlining their central role in cellular patho-physiology. System
539 complexity (connectance $C_v\%$) was strongly correlated with the first Principal Component (PC
540 1, direct), DNA damage (inverse; Comet assay data from Barranger et al., 2019a) and
541 lysosomal stability (direct), as shown in Figure 8A – C (all correlations included data for 0.01
542 and 0.1 mg/L C_{60} from Sforzini et al, 2020). Complexity was also inversely correlated with
543 estimated or predicted programmed cell death (Fig. 8C; predicted PCD was derived from the
544 previously determined correlation between digestive tubule epithelial atrophy and lysosomal
545 stability shown in the inset of Figure 8C; Lowe, 1988; Lowe et al., 1981; Moore 1988).

546

547 *Mixture Interactions*

548 The Interaction Factors (IF) for C_{60} fullerene and BaP are shown in Table 3. There was
549 evidence of antagonistic interactions (t-test, significant at the 5% level) between mixtures of
550 C_{60} fullerene and BaP for DNA damage (Comet, MIX 100 µg/L BaP; data from Barranger et
551 al., 2019a), mTORC1 inhibition, lysosomal membrane stability, lysosomal lipofuscin (MIX 100
552 µg/L BaP), lysosomal lipid (MIX 5 and 50 µg/L BaP), and connectance (Table 3). Furthermore,
553 antagonistic interactions that were just outside the 5% level, but which were significant at the
554 10% level, were also found for lysosomal/cytoplasmic volume ratio (autophagy) with the MIX
555 50 and 100 µg/L BaP, and DNA damage with the MIX 50 µg/L BaP. There was no evidence
556 for any synergistic interactions between the test compounds (Table 3).

557

558 **Discussion**

559 There was no evidence for a synergistic “Trojan Horse” effect when mussels were exposed to
560 mixtures of C₆₀ and BaP. In fact, the converse was observed, with strong evidence for a
561 negative (antagonistic) interaction induced by the combined treatments as has been
562 previously described by Freixa et al. (2018) and Barranger et al. (2019a, b); while Lee et al.,
563 (2011) have shown that C₆₀ was cytoprotective. Canesi et al. (2014) have previously
564 demonstrated both synergistic and antagonistic effects of TiO₂ nanoparticles and TCDD in
565 combination. The findings from these authors indicated an antagonistic effect on lysosomal
566 membrane stability, but that there was a synergistic effect on L/C volume.

567

568 Comparable BaP tissue concentrations in the presence or absence of C₆₀ were observed (Fig.
569 2A); and despite the expected strong sorption of BaP on C₆₀, no Trojan horse effect was
570 observed, and C₆₀-sorbed BaP remained bioavailable (Fig. 2A; Barranger et al., 2019a;
571 Linnard et al., 2017). In general, however, high variability for C₆₀ tissue concentration, as was
572 observed in the MIX 100 µg/L BaP, may conceal subtle changes.

573

574 In a previous study in mussels by Al-Subiai et al. (2012), it has been shown that animals
575 exposed to C₆₀ alone exhibited a higher accumulation of C₆₀ in the digestive gland compared
576 to the gill. Co-exposure to fluoranthene, however, modified the accumulation of C₆₀, with
577 greater accumulation of C₆₀ when animals were exposed to C₆₀ alone compared to the
578 combined exposure.

579

580 When comparing tissue concentrations for BaP and C₆₀, the bioconcentration observed was
581 much lower for C₆₀ compared to BaP. The uptake in the digestive gland of mussels exposed
582 to a similar aqueous concentration of BaP and C₆₀ was about 2000 times higher for BaP.
583 However, non-constant concentrations in the aqueous phase, attributed to sorption and/or
584 sedimentation, did not allow the calculation of bioaccumulation factors, which also requires
585 reaching a steady-state in the tissues (Barranger et al., 2019a). The difference between BaP
586 and C₆₀ tissue concentration could also be attributed to different kinetics of uptake that can in

587 future, only be explored through longer exposure periods and regular sampling. Nonetheless,
588 recent work has indicated a continuous increase of C₆₀ concentrations in whole mussels over
589 at least three weeks (Sanchís et al., 2018). It is probable that the bioavailability of
590 nanomaterials and their co-contaminants depend on many factors such as their size, shape,
591 surface coating and aggregation state and on the metabolism of the species investigated
592 (Linnard et al., 2017).

593

594 C₆₀ fullerene and BaP administered separately is known to accumulate in the mussel digestive
595 gland and to be sequestered in the lysosomal compartment (Barranger et al., 2019a; Sforzini
596 et al., 2018, 2020). This investigation has clearly demonstrated that in animals exposed to the
597 combined BaP and C₆₀ treatments, the PAH and the nanoparticles accumulated in the
598 lysosomes of the digestive gland cells as confirmed with the localisation of the lysosomal
599 marker protease cathepsin-D (Fig. 4A-D). Lysosomal enlargement in molluscan digestive cells
600 is a feature of autophagy. It also involves lysosomal fusion with a decrease in the number of
601 lysosomes (Choy et al., 2018; Lowe et al., 1981). Autophagy is a highly complex process
602 involving the interactions of many proteins and cell signalling pathways (Zhao & Zhang, 2019).
603 The cell pathology results indicate that autophagy is induced in the digestive cells with all
604 experimental treatments as indicated by reduced lysosomal integrity (LMS) and increased
605 lysosomal/cytoplasmic volume ratio.

606

607 C₆₀ accumulates in the lysosomal compartment of molluscan hepatopancreatic digestive cells,
608 probably as a result of endocytic uptake as aggregates or individual nanoparticles, or
609 otherwise adsorbed onto food particles by Van der Waal's interactions (Emelyantsev et al.,
610 2019; Di Giosia et al., 2019; Gieldoń et al., 2017; Rashid et al., 1991; Sforzini et al., 2020).
611 C₆₀ fullerene has been reported to induce autophagy in various cell types, including molluscan
612 digestive cells using LMS, lysosomal volume increase and LC3 (microtubule-associated
613 proteins 1A/1B light chain 3B) as the biomarkers (Lee et al., 2011; Sforzini et al., 2020; Stern
614 et al., 2012). Accumulation of non-degradable C₆₀ in the lysosomal compartment will probably

615 contribute to lysosomal overload and membrane destabilisation with release of iron, and
616 consequent generation of ROS in the cytosol (Sforzini et al., 2020; Stern et al., 2012; Yu et
617 al., 2003). This increased flux of ROS will probably be the major trigger for an augmented
618 autophagic reaction to the nanoparticles by oxidative inhibition (dephosphorylation) of
619 mTORC1 (mechanistic target of rapamycin complex 1; Cuervo, 2004; Moore, 2020).
620 Autophagy induced by C₆₀ appears to be cytoprotective. Although there was some evidence
621 of ROS mediated oxidative damage, such as increased lysosomal fragility, this response was
622 limited and there was no evidence for serious oxidative stress, as would be characterised by
623 the lack of lipofuscin accumulation in the lysosomal compartment (Lee et al., 2011; Moore et
624 al., 2020; Sforzini et al., 2018, 2020; Shaw et al., 2019).

625

626 Accumulation of lysosomal lipofuscin is an effective indicator of oxidative cell injury (Moore et
627 al., 2006; Sforzini et al., 2018). As mentioned above, the C₆₀ treatment did not appear to cause
628 significant oxidative cell injury, as there was no increase in lipofuscin (Sforzini et al., 2020).
629 However, oxidative cell injury was observed in the three BaP treatments, probably caused by
630 increased generation of ROS, accompanied by increased lysosomal lipofuscin and lipid, and
631 reduced lysosomal membrane stability (Fig. 2B, C & D; Fig. 4A, D & E; Jaishy & Abel, 2016;
632 Seranova et al., 2017; Sforzini et al., 2018, 2020). Lipofuscin was elevated in the MIX 5 and
633 50 µg/L BaP treatments. The trend was, however, lower than in the BaP-treated animals and
634 significantly lower at the MIX 100 µg/L BaP ($P \leq 0.05$, Mann-Whitney U-test). It was also
635 significantly antagonistic in the MIX 100 µg/L BaP treatment (Table 3). However, the PCA
636 indicated that this induced autophagy could be differentiated into probable augmented
637 functional autophagy, and augmented but tending towards dysfunctional autophagy (Fig. 6;
638 Moore et al., 2020; Shaw et al., 2019). All of the cellular biomarkers correlated with PC 1
639 (Table 1), whereas PC 2 was strongly correlated with lysosomal lipofuscin and lysosomal lipid
640 content (Table 1), both of which are indicative of dysfunctional autophagy, with inhibition of
641 lysosomal degradative enzymes (Jaishy & Abel, 2016; Shaw et al., 2019). The BaP treated
642 mussels contributed to the alignment with the second principal component (PC 2), while the

643 C₆₀ and mixture treatments aligned with the first principal component (PC 1) as indicated in
644 Figure 8A. The PCA also indicates that there is probably an antagonistic interaction in the
645 mixtures (Fig. 6).

646

647 Excessive lipofuscin accumulation in lysosomes is also harmful in its own right, due to the
648 production of ROS by lipofuscin-bound iron (Brunk & Terman, 2002). Consequently, much of
649 the observed DNA damage will probably have resulted from oxidative injury caused by ROS
650 generated by the release of reactive iron from within the lysosomal compartment, as well as
651 increased ROS produced by iron bound to lysosomal lipofuscin (Barranger et al., 2019a; Brunk
652 & Terman, 2002; Sforzini et al., 2018, 2020; Zanger et al., 2004). There was no evidence for
653 the formation of DNA adducts as a result of interactions with oxidative metabolites of BaP
654 (Barranger et al., 2019a).

655

656 Dysfunctional autophagy characterised by swollen lipid-rich lysosomes (triglyceride lipidosis)
657 can also contribute to an increased level of programmed cell death (Fig. 3D; Cuervo, 2004;
658 Lowe, 1988; Sforzini et al., 2018). This was further reflected as reduced lysosomal membrane
659 stability and associated indications of dysfunctional autophagy was strongly linked with
660 digestive tubule atrophy as a result of programmed cell death (PCD) based on re-analysis of
661 previously published findings (Lowe, 1988; Moore, 1988).

662

663 PCA and cluster analysis, however, does not integrate the various biomarkers in a functionally
664 meaningful way. It is only the first stage in developing numerical and network models for
665 environmental impact on the health of sentinel animals such as mussels and earthworms
666 (Moore, 2010; Sforzini et al., 2015, 2018, 2020). In order to encapsulate the cellular
667 physiological processes, it is necessary to interconnect the biomarker data within a logical
668 mechanistic framework. Previous studies have used a network model of the physiological and
669 pathological processes known to occur in the digestive cells (Moore et al., 2015; Sforzini et
670 al., 2018). Complexity is a measure of the interconnectedness of the network and can be used

671 as an indicator of homeostasis (Lewis et al., 1992; Moore, 2010; Moore et al., 2015; Sedivy,
672 1999). Complexity of the whole system increases when sub-systems, such as detoxication
673 and anti-oxidant protective processes, augmented autophagy, protein degradation and
674 induction of stress proteins, are up-regulated and start to interact significantly as part of a
675 response to low-level stress (i.e., biphasic or hormetic response; Moore, 2010, 2020; Moore
676 et al., 2015, 2020). However, with increasing severity of stress, cell injury and higher-level
677 functional impairment lead to physiological dysfunction, pathology and breakdown of the
678 whole interaction network with consequent loss of complexity (Moore, 2010). Consequently,
679 inputting the biomarker data from the C₆₀ + BaP exposure experiment into a directed cell
680 patho-physiological network model showed that there was a statistically significant reduction
681 in system complexity with increasing tissue BaP (chemical data from Barranger et al., 2019a;
682 Sforzini et al., 2018), in both the presence and absence of C₆₀. This indicated decreased
683 homeostasis and health status (Fig. 5F; Barranger et al., 2019a). The model demonstrates
684 that autophagy is an important highly connected hub in the cellular physiology network of the
685 system being tested. This lends support to the overall hypothesis, namely, that autophagy,
686 lysosomal function, oxidative cell injury and mTOR signalling are intrinsically interlinked in
687 physiological responses and patho-physiological reactions to stress (Fig. 1A). The strong
688 correlations between network complexity versus the first principal component, DNA damage,
689 lysosomal membrane stability and estimated programmed cell death further support the use
690 of system complexity as a measure of cellular homeostasis; and the capability to extrapolate
691 to higher level effects (e.g., predicted PCD; Fig. 8A-D).

692

693 The network approach supports the hypothesis that stress leading to pathology results in a
694 loss of system complexity as previously described by Moore (2010). Consequently, cellular
695 networks can be used to integrate information from biomarker data; and to direct the selection
696 of biomarkers and design of experiments, in order to develop suites of tests that will
697 demonstrate which links are active or inactive, and to what degree. This provides
698 mathematical formalism for an objective evaluation of health status based on measurement of

699 various biomarkers for potential use in risk assessment (Moore, 2010, Moore et al., 2015;
700 Sforzini et al., 2018). The strong correlation between system complexity and DNA damage
701 indicates that this type of modelling has potential for predicting cellular pathological endpoints
702 (Barranger et al., 2019a; Canova et al., 1998; Fig. 1A). DNA damage was included in the
703 network model as an endpoint, although the values from the Comet assays were not required
704 for the calculation of connectance as DNA damage was an endpoint with uni-directional links
705 from oxidative stress and autophagy (Fig. 1B, Table 2).

706

707 Pairwise testing of the BaP and combined (MIX) treatments showed that there were significant
708 decreases at all concentrations of BaP for LMS and mTORC1, while the other biomarkers
709 showed significant decreases at particular concentrations of BaP, but not all (Fig. 5). Network
710 or system complexity was also decreased in the two lower BaP concentration combined
711 treatments (MIX 5 and 50 µg/L BaP; Fig. 5). The autophagy biomarker (L/C volume ratio),
712 however, was increased in the lowest combined treatment (MIX 5 µg/L BaP; Fig. 5). Interaction
713 factors (I_{fs}) generally indicated that cell injury was statistically additive at MIX 5 and 50 µg/L
714 BaP, but was antagonistic at MIX 100 µg/L BaP, based on the lipofuscin levels (Table 3).
715 There appeared, however, to be an intracellular limiting effect on oxidative cell injury in some
716 of the test mixture treatments, as exemplified by the antagonistic interactions for DNA damage
717 (MIX 100 µg/L BaP), phosphorylated mTORC1 kinase, LMS, lysosomal lipofuscin (MIX 100
718 µg/L BaP) and lysosomal lipid accumulation (MIX 100 µg/L BaP; Table 3). The additional
719 evidence from the PCA and network analyses support the interpretation that this amelioration
720 in cell injury in the mixtures may be caused either by a reduction in ROS generation, or else
721 by more effective scavenging of ROS by C₆₀, when C₆₀ and BaP are present together in close
722 association, as previously described (Della Torre et al. 2018; Di et al. 2017). C₆₀ fullerenes are
723 both cytoprotective scavengers and generators of ROS (Barranger et al., 2019a; Lee et al.,
724 2011; Rondags et al., 2017; Sforzini et al., 2020); and when C₆₀ fullerene and BaP are closely
725 associated, or bound together, within the overloaded lysosomal compartment of the mussel

726 digestive cells, the ROS scavenging ability of C₆₀ is probably a significant factor (Fig. 9A-C;
727 Barranger et al., 2019; Stern et al., 2012).

728

729 Uptake of both BaP and C₆₀ is probably mediated by endocytosis, associated with food
730 proteins or else bound to cell surface proteins mediated by Van der Waals interaction
731 (Emelyantsev et al., 2019; Di Giosia et al., 2019; Gieldoń et al., 2017; González-Soto et al.,
732 2019; Moore et al., 2004; Oh & Park, 2014; Rashid et al., 1991; Sayes et al., 2004). BaP may
733 also enter the digestive cells through a combination of direct transfer (Plant et al., 1985); as
734 well as through endocytosis in bound form with C₆₀ and food proteins and lipids (Barranger et
735 al., 2019a; Sforzini et al., 2018). However, mTORC1 is inhibited by ROS and oxidative
736 damage, which will probably limit endocytic uptake of particle associated BaP and C₆₀ + bound
737 BaP (Zhao et al., 2017). Inhibition of mTORC1 will also trigger decreased LMS, as well as
738 increased autophagy and programmed cell death (i.e., PCD type 1 – apoptosis, PCD type 2 –
739 autophagic cell death and PCD type 3 – necrotic cell death; Cuervo, 2004; Seo et al., 2018;
740 Wang et al., 2018). Previous studies have shown that PAHs such as fluoranthene, 3-
741 methylcholanthrene and BaP accumulate in the lysosomal compartment; where they
742 destabilise the lysosomal membrane releasing lysosomal iron, hence, inducing oxidative cell
743 injury and dysfunctional autophagy in the hepatopancreatic digestive cells (Kurz et al., 2008;
744 Moore et al., 2006, 2007; Sforzini et al., 2018; Shaw et al., 2019; Stern et al., 2012). Autophagy
745 and lysosomal function can become dysfunctional due to excessive lipid and lipofuscin
746 accumulation (Brunk & Terman, 2002; Jaishy & Abel, 2016; Kurz et al., 2008).

747

748 There was strong evidence for interactions in the biomarker and connectance data for the
749 three combinations of BaP and C₆₀ fullerene (Barranger et al., 2019a, b; David et al., 2016;
750 Katsifis et al., 1996; Schlesinger et al., 1992; Zhang et al., 2019). The antagonistic interactions
751 reported here can be interpreted as a cytoprotective effect against the cytotoxicity of BaP
752 being exerted by C₆₀ scavenging of ROS generated by BaP overload within the lysosomal
753 compartment (Barranger et al., 2019a, b; David et al., 2016; Katsifis et al., 1996; Lee et al.,

2011; Schlesinger et al., 1992; Sforzini et al., 2018; Stern et al., 2012; Zhang et al., 2019). Augmented autophagy induced by oxidative inhibition of mTORC1 will also have contributed to the cytoprotective effect of C₆₀ (Lee et al., 2011; Moore, 2020; Moore et al., 2020; Sforzini et al., 2020). However, C₆₀ does also exert cytotoxicity in its own right, so the cytoprotective properties appear to be superimposed on the toxicity of BaP when the two compounds are used in combination (Fig. 9A-C). C₆₀ is known to have cytoprotective properties as well as being a generator of ROS (Rondags et al., 2017; Zhang et al., 2019). Since ROS generation by C₆₀ is induced by visible light, it is considered unlikely that C₆₀ is producing significant ROS within the lysosomal-vacuolar system of the digestive cells: rather the sequestration of non-degradable C₆₀ in the lysosomes will cause limited release of intra-lysosomal iron that will in turn, generate ROS and inhibit mTORC1, thus triggering protective augmented autophagy (Kirchin et al., 1992; Moore, 2020; Moore et al., 2020; Sforzini et al., 2020; Stern et al., 2012; Winston et al., 1991; Zhao & Zhang, 2019). The findings of Barranger et al. (2019a) and the current data support the cytoprotective interpretation of internalised C₆₀ nanoparticles (Fig. 8C). In fact, the chemical analytical data reported by Barranger et al. (2019a) indicated that the internalisation of C₆₀ was considerably enhanced when mussels were treated at the highest experimental concentration of BaP (100 µg/L), in comparison with the lower treatment concentrations (Fig 2B). The explanation for this is not readily apparent, however, the chemical data for C₆₀ + BaP (100 µg/L) had high variability (Fig. 2B; Barranger et al., 2019a).

773

The digestive gland, liver analogue, is probably the most important organ for the health of the mussel. Damage to this organ, as described in this investigation, has the potential for serious higher level adverse impacts on the functionality of the whole animal. This cell injury, in turn, will have potential eco-pathological consequences for the mussel population and functional ecology of the ecological assemblages that are dependent on mussels as ecological foundation species (Moore et al., 2013).

780

781 The network modelling has facilitated the further refinement of an integrated conceptual
782 mechanistic framework described by Sforzini et al. (2018) that encapsulates the interrelated
783 patho-physiological processes involved in the cellular reactions to C₆₀ and BaP. These
784 processes have been described diagrammatically in Figure 10, and in a network format in
785 Figure 1A. Although most of these processes are considered to be evolutionarily highly
786 conserved, some have not yet been confirmed to occur in molluscs (i.e., mTORC1 links with
787 the regulation of endocytosis and MDR/Pgp40 multi-drug resistance transporter) (Boya, 2012;
788 Flinn & Backer, 2010; Grahammer et al., 2016; Jiang & Liu, 2008; Wang et al., 2018).
789 Physiological augmented autophagy is activated by the inhibition of mTORC1, along with
790 reduced lysosomal membrane permeability or LMS. This can be triggered by a number of
791 environmental factors, including low nutrient concentration and oxidative stress (Moore et al.,
792 2007; Seranova et al., 2017; Zhao et al., 2017).

793

794 As previously described, hypothesised functional links between endocytic uptake of C₆₀ and
795 BaP with natural particles, transfer to the lysosomal system, where accumulation will be further
796 facilitated by the presence of P-glycoprotein (MDR-Pgp40) in the lysosomal membrane (Minier
797 & Moore, 1996a, b; Yang et al., 2002). The demonstrated accumulation of C₆₀ fullerene, BaP
798 and lipid in the lysosomal compartment will probably result in ROS generation and formation
799 of lipofuscin or stress/age pigment (Brunk & Terman, 2002; Moore et al., 2006; Sforzini et al.,
800 2018). However, C₆₀ fullerene is indicated to have a cytoprotective role in scavenging ROS
801 generated by BaP in the mixture treatments as shown diagrammatically in Figure 6. mTORC1
802 inhibition by ROS is probably a further contributory factor to cytoprotection in the C₆₀ + BaP
803 mixtures as this inhibition will result in augmented functional autophagy, whereas BaP on its
804 own will shift the balance towards dysfunctional autophagy (Fig. 9A-C; Moore et al., 2020;
805 Sforzini et al., 2018, 2020; Shaw et al., 2019).

806

807 The network model shown in Figure 1A and B indicates that lysosomal function and autophagy
808 are both highly connected nodes, and as such form important hubs in the cellular physiology

809 of the digestive cells. Consequently, physiological hub dysfunction as a result of xenobiotic
810 and NP overload and the associated oxidative attack, is indicative of the importance of both
811 these linked modular cellular systems to the normal functioning of the digestive cells as well
812 as in the cell's response to stress (Stern et al., 2012). The relative homogeneity of the
813 responses of network complexity responses (connectance) to the experimental treatments as
814 shown in Figure 5F, indicates that the animals are effectively compensating for the
815 environmental insults and have established a new steady state (Moore, 2010; Stelling et al.,
816 2004). An explanation for this may be that even if individual nodes (vertices) are compromised,
817 the system or network can compensate by bypassing or modifying the interaction strengths
818 for the damaged node, and utilise alternative processes and pathways to minimise network
819 disruption and the degree of cell injury (Fig. 1A; Stelling et al., 2004). Stelling et al. (2004) has
820 previously demonstrated that functional cellular networks are highly robust when perturbed by
821 environmental and other stressors, and will establish a new physiological state unless a key
822 hub (highly connected node) or several hubs is compromised.

823

824 In the future, the individual nodes in the network representing cellular processes can
825 potentially be further modelled at lower levels of biological organisation by inputting
826 transcriptomic and proteomic data as has been initiated by Banni et al. (2017) and Barranger
827 et al. (2019a,b). This capability will probably be enhanced by future improvements in our
828 knowledge of protein-protein interactions (interactome); as well as how effectively gene
829 expression correlates with the proteome and is represented by functional interacting proteins.
830 However, at present the pathways that regulate the kinetics of transcriptional and translational
831 activity and post-translational modification of proteins during cell maturation are not well
832 defined (Hoogendijk et al., 2019). In addition, the often low correlation between the
833 transcriptome and the proteome supports the view that post-transcriptional processes play a
834 major role in the adaptation to altered physiological conditions (Bathke et al., 2019).

835

836 **Conclusions**

837 The hypothesis that C₆₀ fullerene exerts an antagonistic interactive effect on the toxicity of
838 benzo[a]pyrene has been supported by this investigation. BaP and C₆₀ were shown to co-
839 localise in the secondary lysosomes of the hepatopancreatic digestive cells in the digestive
840 gland. Combinations of BaP and C₆₀ showed antagonistic effects for lysosomal membrane
841 stability, mTORC1 inhibition, lysosomal lipofuscin and lysosomal lipid (MIX 5 & 50 µg/L BaP).
842 Previous reports based on data from the same investigation have indicated an antagonistic
843 interaction for DNA damage. The biomarker data analysed using multivariate statistics:
844 principal component and cluster analysis clearly showed that BaP on its own was more
845 injurious than when in combination with C₆₀. When the biomarker data were incorporated in
846 an interactive network model describing the main cell pathology processes, the integrated
847 outputs (connectance – C_v%) for the system complexity (i.e., essentially a measure of system
848 integrity or homeostasis) showed that there was a significant antagonistic interaction at all
849 BaP concentrations for the combined treatments. It is inferred that oxidative cell injury
850 reactions induced by BaP are ameliorated in the combination treatments by the ROS
851 scavenging property of intralysosomal C₆₀. This limits the injury to the lysosomal membrane,
852 reducing the oxidative damage in the cytosol and to the DNA. The ROS scavenging by C₆₀ in
853 combination with enhanced autophagic turnover of damaged cell constituents appears to have
854 a cytoprotective effect against the toxic reaction to BaP in the combined treatments

855

856 Furthermore, the loss of cellular physiological complexity in the hepatopancreatic digestive
857 cells, has a potential predictive capability, since complexity correlated inversely with DNA
858 damage. It also inversely correlated with the degree of predicted PCD caused by the
859 experimental treatments based on the inverse correlation between lysosomal membrane
860 stability and digestive tubule atrophy. The network model deployed in this investigation and a
861 previous study of the effects of BaP is a subset of a larger network model incorporating other
862 processes that were not included in this study, but that are known to be involved in the patho-
863 physiology and induced molecular toxicology of mussels. It is suggested that the inclusion of
864 a larger group of molecular and cellular biomarkers in future studies, as indicated in this larger

865 network, will give a more comprehensive picture of the cellular dysfunctionality caused by
866 environmental nanomaterials and toxic xenobiotics in the molluscan digestive gland
867 (hepatopancreas) following environmental insult.

868

869 **Acknowledgements**

870 This study was supported financially by the Natural Environment Research Council (NERC),
871 UK (Grant No.NE/L006782/1; PI: ANJ). There are no conflicts of interest.

872

873 **References**

- 874 Al-Subiai, S.N., Arlt, V.M., Frickers, P.E., Readman, J.W., Stolpe, B., Lead, J.R., Moody, A.J.,
875 Jha, A.N., 2012. Merging nano-genotoxicology with eco-genotoxicology: An integrated
876 approach to determine interactive genotoxic and sub-lethal toxic effects of C₆₀ fullerenes
877 and fluoranthene in marine mussels, *Mytilus* sp. *Mutat. Res. Genet. Toxicol. Environ.*
878 *Mutagen.*, 745, 92–103.
- 879 Banni, M., Sforzini, S., Arlt, V.M., Barranger, A., Dallas, L.J., Oliveri, C., Aminot, Y., Pacchioni,
880 B., Millino, C., Lanfranchi, G., Readman, J.W., Moore, M.N., Viarengo, A., Jha, A.N.,
881 2017. Assessing the impact of Benzo[a]pyrene on Marine Mussels: Application of a
882 novel targeted low density microarray complementing classical biomarker responses.
883 *PLoS One* 12(6):e0178460. doi: 10.1371/journal.pone.0178460.
- 884 Barranger, A., Langan, L.M., Sharma, V., Rance, G.A., Aminot, Y., Weston, N.J., Akcha, F.,
885 Moore, M.N., Arlt, V.M., Khlobystov, A.N., Readman, J.W., Jha, A.N., 2019a.
886 Antagonistic interactions between benzo[a]pyrene and fullerene (C₆₀) in toxicological
887 response of marine mussels. *Nanomaterials (Basel)* 8;9(7). pii: E987. doi:
888 10.3390/nano9070987.
- 889 Barranger, A., Rance, G.A., Aminot, Y., Dallas, L.J., Sforzini, S, Weston, N.J., Lodge, R.W.,
890 Banni, M., Arlt, V.M., Moore, M.N., Readman, J.W., Viarengo, A., Khlobystov, A.N., Jha,
891 A.N., 2019b. An integrated approach to determine interactive genotoxic and global gene
892 expression effects of multiwalled carbon nanotubes (MWCNTs) and benzo[a]pyrene

893 (BaP) on marine mussels: evidence of reverse 'Trojan Horse' effects. *Nanotoxicology*
894 13, 1324-1343.

895 Bathke, J., Konzer, A., Remes, B., McIntosh, M., Klug, G., 2019. Comparative analyses of
896 the variation of the transcriptome and proteome of *Rhodobacter sphaeroides*
897 throughout growth. *BMC Genomics* 20, 358; [https://doi.org/10.1186/s12864-019-5749-](https://doi.org/10.1186/s12864-019-5749-3)
898 3.

899 Bignell, J.P., Stentiford, G.D., Taylor, N.G., Lyons, B.P., 2011. Histopathology of mussels
900 (*Mytilus* sp.) from the Tamar estuary, UK. *Mar. Environ. Res.*, 72(1-2), 25-32.

901 Bonchev, D., 2003. Complexity of protein-protein interaction networks, complexes, and
902 pathways. In: *Handbook of proteomic methods* (Ed. P.M. Conn) pp. 451-462. Humana
903 Press, Totowa, New Jersey.

904 Boya, P., 2012. Lysosomal function and dysfunction: mechanism and disease. *Antiox. Redox*
905 *Signaling* 17, 766-774.

906 Brunk, U.T., Terman, A., 2002. Lipofuscin: mechanisms of age-related accumulation and
907 influence on cell function. *Free Rad. Biol. Med.* 33, 11-619.

908 Buckland-Nicks, J., Hodgson, A.N., 2005. Paraspermatogenesis of cerithioidean snails:
909 retention of an acrosome and nuclear remnant. *J. Morphology* 264, 314-326.

910 Buzatto, B.A., Kotiaho, J.S., Tomkins, J.L., Simmons, L.W., 2015. Intralocus tactical conflict:
911 genetic correlations between fighters and sneakers of the dung beetle *Onthophagus*
912 *taurus*. *J. Evolut. Biol.*, 28, 730-738.

913 Canesi, L., Frenzilli, G., Balbi, T., Bernardeschi, M., Ciacci, C., Corsolini, S., Della Torre,
914 C., Fabbri, R., Faleri, C., Focardi, S., Guidi, P., Kočan, A., Marcomini, A., Mariottini, M.,
915 Nigro, M., Pozo-Gallardo, K., Rocco, L., Scarcelli, V., Smerilli, A., Corsi, I., 2014.
916 Interactive effects of n-TiO₂ and 2,3,7,8-TCDD on the marine bivalve *Mytilus*
917 *galloprovincialis*. *Aquatic Toxicol.*, 153, 53-65.

918 Canova, S., Degan, P., Peters, L.D., Livingstone, D.R., Voltan, R., Venier, P., 1998. Tissue
919 dose, DNA adducts, oxidative DNA damage and CYP1A-immunopositive proteins in

920 mussels exposed to waterborne benzo[a]pyrene. *Mutation Res/Fundamental and*
921 *Molecular Mechanisms of Mutagenesis* 399, 17-30.

922 Chen, L., Xu, B., Liu, L., Luo, Y., Yin, J., Zhou, H., Chen, W., Shen, T., Han, X., Huang, S.,
923 2010. Hydrogen peroxide inhibits mTOR signaling by activation of AMPK α leading to
924 apoptosis of neuronal cells. *Lab. Invest.* 90, 762-773.

925 Choy, C.H., Saffi, G., Gray, M.A., Wallace, C., Dayam, R.M., Ou, Z.-Y.A., Lenk,
926 G., Puertollano, R., Watkins, S.C., Botelho, R.J., 2018. Lysosome enlargement during
927 inhibition of the lipid kinase PIKfyve proceeds through lysosome coalescence. *J. Cell*
928 *Sci.*, 131(10), jcs213587. doi:10.1242/jcs.213587.

929 Clarke, K.R., 1999. Non-metric multivariate analysis in community-level ecotoxicology.
930 *Environ. Toxicol. Chem.* 18, 117-127.

931 Clarke, K.R., Warwick, R.M., 2001. Change in marine communities: an approach to statistical
932 analysis and interpretation. PRIMER- ϵ , Plymouth, UK.

933 Cuervo, A.M. (2004) Autophagy: in sickness and in health. *TRENDS Cell Biol.*, 14, 70-77.

934 David, R., Ebbels, T., Gooderham, N., 2016. Synergistic and antagonistic mutation responses
935 of human MCL-5 cells to mixtures of benzo[a]pyrene and 2-amino-1-methyl-6-
936 phenylimidazo[4,5-*b*]pyridine: dose-related variation in the joint effects of common
937 dietary carcinogens. *Environ. Health Perspect.*, 124, 88-96.

938 Davis, M.W., 1997. Complexity formalisms, order and disorder in the structure of art. In:
939 *Evolutionary Programming VI, Lecture Notes in Computer Science* (Editors: Angeline
940 PJ, Reynolds, McDonnell JR, Eberhart R), Vol. 1213, Springer International Publishing
941 AG, Switzerland. pp 1-12.

942 D'Agata, A., Fasulo, S., Dallas, L.J., Fisher, A.S., Maisano, M., Readman, J.W., Jha, A.N.,
943 2014. Enhanced toxicity of 'bulk' titanium dioxide compared to 'fresh' and 'aged' nano-
944 TiO₂ in marine mussels (*Mytilus galloprovincialis*). *Nanotoxicology*, 8, 549-558.

945 De Duve, C., De Barse, T, Poole, B., Trouet, A., Tulkens, P., Van Hoof, F., 1974. Commentary.
946 Lysosomotropic agents. *Biochem. Pharmacol.*, 23, 2495–2531.

947 Della Torre, C., Maggioni, D., Ghilardi, A., Parolini, M., Santo, N., Landi, C., Madaschi, L.,
948 Magni, S., Tasselli, S., Ascagni, M., Bini, L., La Porta, C., Del Giacco, L., Binelli, A.,
949 2018. The interactions of fullerene C₆₀ and benzo[*a*]pyrene influence their bioavailability
950 and toxicity to zebrafish embryos. *Environ. Pollut.*, 241, 999-1008.

951 Di Giosia, M., Valle, F., Cantelli, A., Bottoni, A., Zerbetto, F., Calvaresi, M., 2018. C₆₀
952 bioconjugation with proteins: towards a palette of carriers for all pH ranges. *Materials*
953 2018, 11, 691; doi:10.3390/ma11050691.

954 Di Giulio, R.T., Hinton, D.E., Editors, 2008. *The toxicology of fishes*. Taylor and Francis,
955 London, New York, Singapore, Melbourne, 1071 p.

956 Di, Y., Aminot, Y., Schroeder, D.C., Readman, J.W., Jha, A.N., 2017. Integrated biological
957 responses and tissue-specific expression of *p53* and *ras* genes in marine mussels
958 following exposure to benzo(*a*)pyrene and C₆₀ fullerenes, either alone or in combination.
959 *Mutagenesis* 32, 77-90.

960 Di, Y., Schroeder, D.C., Highfield, A., Readman, J.W., Jha, A.N., 2011. Tissue specific
961 expression of *p53* and *ras* genes in response to the environmental genotoxicants
962 Benzo(*a*)pyrene in marine mussels. *Environmental Science and Technology* 45, 8974-
963 8981.

964 Dodd, N.J.F., Jha, A.N., 2009. Titanium dioxide induced cell damage: A proposed role of the
965 carbonyl radical. *Mutation Research (Fundamental and Molecular Mechanisms of*
966 *Mutagenesis)*, 660, 79-82.

967 Eichmüller, S., Stevenson, P. A., Paus, R., 1996. A new method for double immunolabelling
968 with primary antibodies from identical species. *J. Immunol. Methods*, 190, 255-265.

969 Emelyantsev, S., Prazdnova, E., Chistyakov, V., Alperovich, I., 2019. Biological effects of C₆₀
970 fullerene revealed with bacterial biosensor—toxic or rather antioxidant? *Biosensors*, 9,
971 81; doi:10.3390/bios9020081.

972 Flinn, R.J., Backer, J.M., 2010. mTORC1 signals from late endosomes: taking a TOR of the
973 endocytic system. *Cell Cycle*, 9, 1869-1870.

974 Freixa, A., Acuna, V., Sanchis, J., Farre, M., Barcelo, D., Sabater, S., 2018. Ecotoxicological
975 effects of carbonbased nanomaterials in aquatic organisms. *Sci. Total Environ.*, 619-
976 620, 328-337.

977 Gieldoń, A., Witt, M.M., Gajewicz, A., Puzyn, T., 2017. Rapid insight into C₆₀ influence on
978 biological functions of proteins. *Structural Chemistry*, 28:1775–1788.

979 Giese, B., Klaessig, F., Park, B., Kaegi, R., Steinfeldt, M., Wigger, H., Von Gleich, A.,
980 Gottschalk, F., 2018. Risks, release and concentrations of engineered nanomaterials in
981 the environment. *Scientific Reports*, 8(1), 1565. doi:10.1038/s41598-018-19275-4.

982 González-Soto, N., Hatfield, J., Katsumiti, A., Duroudier, N., Lacave, J.M., Bilbao, E., Orbea,
983 A., Navarro, E., Cajaraville, M.P., 2019. Impacts of dietary exposure to different sized
984 polystyrene microplastics alone and with sorbed benzo[a]pyrene on biomarkers and
985 whole organism responses in mussels *Mytilus galloprovincialis*. *Sci. Tot. Environ.*, 684,
986 548-566.

987 Grahammer, F., Ramakrishnan, S. K., Rinschen, M. M., Larionov, A. A., Syed, M., Khatib, H.,
988 Roerden, M., Sass, J. O., Helmstaedter, M., Osenberg, D., Kühne, L., Kretz, O., Wanner,
989 N., Jouret, F., Benzing, T., Artunc, F., Huber, T. B., Theilig, F. (2016). mTOR regulates
990 endocytosis and nutrient transport in proximal tubular cells. *J. Am. Soc. Nephrol.*, 28,
991 230-241.

992 Halenova, T., Raksha, N., Vovk, T., Savchuk, O., Ostapchenko, L, Prylutsky, Y., Kyzyma, O.,
993 Ritter, U., Scharff, P., 2018. Effect of C₆₀ fullerene nanoparticles on the diet-induced
994 obesity in rats. *Int J Obes* 42, 1987–1998.

995 Hoogendijk, A.J., Pourfarzad, F., Aarts, C.E.M., Tool, A.T.J., Hiemstra, I.H., Grassi, L.,
996 Frontini, M., Meijer, A.B., van den Biggelaar, M., Kuijpers, T.W., 2019. Dynamic
997 transcriptome-proteome correlation networks reveal human myeloid differentiation and
998 neutrophil-specific programming. *Cell Reports*, 29, 2505–2519.

999 Jaishy, B., Abel, E.D., 2016. Lipids, lysosomes, and autophagy. *Journal of Lipid Research*,
1000 57, 1619–1635.

1001 Jeong, H., Tombor, B., Albert, R., Oltval, Z.N., Barábasi, A.-L., 2000. The large scale
1002 organization of metabolic networks. *Nature* 407, 651-654.

1003 Jiang, B.H., Liu, L.Z., 2008. Role of mTOR in anticancer drug resistance: perspectives for
1004 improved drug treatment. *Drug Resist. Updates* 11, 63-76.

1005 Jimeno-Romero, A., Oron, M., Cajaraville, M.P., Soto, M., Marigomez, I., 2016. Nanoparticle
1006 size and combined toxicity of TiO₂ and DSLS (surfactant) contribute to lysosomal
1007 responses in digestive cells of mussels exposed to TiO₂ nanoparticles. *Nanotoxicology*,
1008 10, 1168–1176.

1009 Juste, Y.R., Cuervo, A.M., 2019. Analysis of Chaperone-Mediated Autophagy. *Methods Mol.*
1010 *Biol.*, 1880, 703-727. doi:10.1007/978-1-4939-8873-0_47

1011 Katsifis, S.P., Kinney, P.L., Hosselet, S., Burns, F.J., Christie, N.T., 1996. Interaction of nickel
1012 with 537 mutagens in the induction of sister chromatid exchanges in human
1013 lymphocytes. *Mutat. Res.*, 359, 7-15.

1014 Kirchin, M.A., Moore, M.N., Dean, R.T. and Winston, G.W., 1992. The role of oxyradicals in
1015 intracellular proteolysis and toxicity in mussels. *Mar. Environ. Res.*, 34, 315-320.

1016 Koehler, A., Marx, U., Broeg, K., Bahns, S., Bressling, J., 2008. Effects of nanoparticles in
1017 *Mytilus edulis* gills and hepatopancreas - a new threat to marine life? *Mar. Environ. Res.*,
1018 66, 12–14.

1019 Kurz, T., Terman, A., Gustafsson, B., Brunk, U.T., 2008. Lysosomes in iron metabolism,
1020 ageing and apoptosis. *Histochemistry & Cell Biology*, 29, 389-406.

1021 Lee, D., Hong, J.H., 2020. Nanoparticle-mediated therapeutic application for modulation of
1022 lysosomal ion channels and functions. *Pharmaceutics*, 12, 217; doi:10.3390/
1023 pharmaceutics12030217.

1024 Lee, C.M., Huang, S.T., Huang, S.H., et al., 2011. C₆₀ fullerene-pentoxifylline dyad
1025 nanoparticles enhance autophagy to avoid cytotoxic effects caused by the β -amyloid
1026 peptide. *Nanomedicine*, 7(1), 107-114.

1027 Levine B (2005) Eating oneself and uninvited guests: autophagy-related pathways in cellular
1028 defense. *Cell*, 120, 159-162.

1029 Lewis, A., Lipsitz, M.D., Ary, L., Goldberger, M.D., 1992. Loss of “complexity” and aging:
1030 potential applications of fractals and chaos theory to senescence. J. Amer. Med. Assoc.
1031 267, 1806-1809.

1032 Livingstone, D.R., Chipman, J.K., Lowe, D.M., Minier, C., Mitchelmore, C.L., Moore, M.N.,
1033 Peters, L.D., Pipe, R.K., 2000. Development of biomarkers to detect the effects of
1034 organic pollution on aquatic invertebrates: recent molecular, genotoxic, cellular and
1035 immunological studies on the common mussel (*Mytilus edulis* L.) and other mytilids. Int.
1036 J. Environ. Pollut. 13, 56-91.

1037 Lowe, D.M., 1988. Alterations in cellular structure of *Mytilus edulis* resulting from exposure to
1038 environmental contaminants under field and experimental conditions. Mar. Ecol. Prog.
1039 Ser. 46, 91-100

1040 Lowe, D.M., Moore, M.N., 1979. The cytochemical distributions of zinc (Zn II) and iron (Fe III)
1041 in the common mussel, *Mytilus edulis*, and their relationship with lysosomes. J. mar. biol.
1042 Ass. U.K., 59, 851-858.

1043 Lowe, D.M., Moore, M.N., Clarke, K.R., 1981. Effects of oil on digestive cells in mussels:
1044 quantitative alterations in cellular and lysosomal structure. Aquatic Toxicol., 1, 213-226.

1045 Markovic, Z., Trajkovic, V. 2008. Biomedical potential of the reactive oxygen species
1046 generation and quenching by fullerenes (C₆₀). Biomaterials, 29, 3561–3573.

1047 Minier, C., Moore, M.N., 1996a. Multixenobiotic resistance in mussel blood cells. Mar. Environ.
1048 Res. 42, 389-392.

1049 Minier, C., Moore, M.N., 1996b. Rhodamine B accumulation and MXR protein expression in
1050 mussel blood cells: effects of exposure to vincristine. Mar. Ecol. Prog. Ser. 142, 165-
1051 173.

1052 Mochida, K., Oikawa, Y., Kimura, Y., Kirisako, H., Hirano, H., Ohsumi, Y., Nakatogawa, H.,
1053 2015. Receptor-mediated selective autophagy degrades the endoplasmic reticulum and
1054 the nucleus. Nature 522, 59-362.

1055 Moore, M.N., 1988. Cytochemical responses of the lysosomal system and NADPH-
1056 ferrihemoprotein reductase in molluscs to environmental and experimental exposure to
1057 xenobiotics. *Mar. Ecol. Prog. Ser.*, 46, 81-89.

1058 Moore, M.N., 2010. Is toxicological pathology characterised by a loss of system complexity?
1059 *Mar. Environ. Res.* 69, S37-S41.

1060 Moore, M.N., 2020. Lysosomes, autophagy and hormesis in cell physiology, pathology and
1061 age-related disease. *Dose Response*, 2020; DOI: 10.1177/1559325820934227.

1062 Moore, M.N., Allen, J.I. & McVeigh, A., 2006. Environmental prognostics: an integrated model
1063 supporting lysosomal stress responses as predictive biomarkers of animal health status.
1064 *Mar. Environ. Res.*, 61, 278–304.

1065 Moore, M.N., Depledge, M.H., Readman, J.W., Leonard, P., 2004. An integrated biomarker-
1066 based strategy for ecotoxicological evaluation of risk in environmental management.
1067 *Mutation Res.*, 552, 247-268.

1068 Moore, M.N., Koehler, A., Lowe, D. & Viarengo, A., 2008. Lysosomes and autophagy in
1069 aquatic animals. In: *Methods in Enzymology* (D.Klionsky, Ed), 451, 582-620. Academic
1070 Press/Elsevier, Burlington.

1071 Moore, M.N., Readman, J.A., Readman, J.W., Lowe, D.M., Frickers, P.E., Beesley, A., 2009.
1072 Lysosomal cytotoxicity of carbon nanoparticles in cells of the molluscan immune system:
1073 an *in vitro* study. *Nanotoxicology*, 3, 40-45.

1074 Moore, M.N., Shaw, J.P., Ferrar Adams, D.R., Viarengo, A., 2015. Anti-oxidative cellular
1075 protection effect of fasting-induced autophagy as a mechanism for hormesis. *Mar.*
1076 *Environ. Res.* 107, 35-44.

1077 Moore, M.N., Shaw, J.P., Pascoe, C., Beesley, A., Viarengo, A., Lowe, D.M., 2020. Anti-
1078 oxidative hormetic effects of cellular autophagy induced by nutrient deprivation in a
1079 molluscan animal model. *Marine Environmental Research*, 156, 104903;
1080 <https://doi.org/10.1016/j.marenvres.2020.104903>.

1081 Moore, M.N., Viarengo, A., Donkin, P., Hawkins, A.J.S., 2007. Autophagic and lysosomal
1082 reactions to stress in the hepatopancreas of blue mussels. *Aquatic Toxicol.*, 84, 80-
1083 91.

1084 Moore, M.N., Viarengo, A.G., Somerfield, P.J., Sforzini, S., 2013. Linking lysosomal
1085 biomarkers and ecotoxicological effects at higher biological levels. In - *Ecological*
1086 *Biomarkers: Indicators of Ecotoxicological Effects*, (Eds.C. Amiard-Triquet, J.C. Amiard,
1087 P.S. Rainbow), pp. 107-130. CRC Press, Boca Raton (Florida), New York & Oxford.

1088 Nakamura, S., Yoshimori, T., 2017. New insights into autophagosome-lysosome fusion. *J.*
1089 *Cell Sci.*,130(7), 1209-1216.

1090 Oh, N., Park, J.H., 2014. Endocytosis and exocytosis of nanoparticles in mammalian cells. *Int.*
1091 *J. Nanomedicine*, 6;9 Suppl 1(Suppl 1):51-63. doi: 10.2147/IJN.S26592. PMID:
1092 24872703; PMCID: PMC4024976.

1093 Plant, A.L., Benson, D.M., Smith, L.C., 1985. Cellular uptake and intracellular localization of
1094 benzo(a)pyrene by digital fluorescence imaging microscopy. *J. Cell Biol.*, 100, 1295-
1095 1308.

1096 Rashid, F., Horobin, R.W., Williams, M.A., 1991. Predicting the behaviour and selectivity of
1097 fluorescent probes for lysosomes and related structures by means of structure-activity
1098 models. *Histochem. J.*, 23, 450-459.

1099 Reeves JF, Davies, S.J., Dodd N.J.F., Jha, A.N., 2008. Hydroxyl radicals ($\cdot\text{OH}$) are associated
1100 with titanium dioxide (TiO_2) nanoparticle-induced cytotoxicity and oxidative DNA
1101 damage in fish cells. *Mutation Research (Fundamental and Molecular Mechanisms of*
1102 *Mutagenesis)*, 640, 113-122.

1103 Rondags, A., Yuen, W.Y., Jonkman, M.F., Horváth, B., 2017. Fullerene C_{60} with cytoprotective
1104 and cytotoxic potential: prospects as a novel treatment agent in Dermatology? *Exp.*
1105 *Dermatol.*, 26, 220-224.

1106 Sanchís, J., Aminot, Y., Abad, E., Jha, A.N., Readman, J.W., Farré, M., 2018. Transformation
1107 of C_{60} fullerene aggregates suspended and weathered under realistic environmental
1108 conditions. *Carbon*, 128, 54–62.

1109 Sayes, C.M., Fortner, J.D., Guo, W., Lyon, D., Boyd, A.M., Ausman, K.D., Tao, Y.J.,
1110 Sitharaman, B., Wilson, L.J., Hughes, J.B., West, J.L., Colvin, V.L., 2004. The differential
1111 cytotoxicity of water-soluble fullerenes. *Nano Letters*, 4, 1881-1887.

1112 Schlesinger, R.B., Zelikoff, J.T., Chen, L.C., Kinney, P.L., 1992. Assessment of toxicologic
1113 interactions resulting from acute inhalation exposure to sulfuric acid and ozone mixtures.
1114 *Toxicol. Appl. Pharmacol.*, 115, 183-190.

1115 Sedivy, R., 1999. Chaodynamic loss of complexity and self-similarity cancer. *Med.*
1116 *Hypotheses* 52, 271-274.

1117 Seo, S.U., Woo, S.M., Kim, S.H., Min, K.-J. & Kwon, T.K., 2018. mTORC1/2 inhibitor and
1118 curcumin induce apoptosis through lysosomal membrane permeabilization-mediated
1119 autophagy. *Oncogene*, 37, 5205-5220.

1120 Seranova, E., Connolly, K.L., Zatyka, M., Rosenstock, T.R., Barrett, T., Tuxworth, R.I., Sarkar,
1121 S., 2017. Dysregulation of autophagy as a common mechanism in lysosomal storage
1122 diseases. *Essays Biochem.*, 61, 733-749.

1123 Sforzini, S., Moore, M.N., Boeri, M., Bencivenga, M., Viarengo, A., 2015. Effects of PAHs and
1124 dioxins on the earthworm *Eisenia andrei*: a multivariate approach for biomarker
1125 interpretation. *Environ. Pollut.*, 196, 60-71.

1126 Sforzini, S., Moore, M.N., Oliveri, C., Volta, A., Jha, A., Banni, M., Viarengo, A., 2018. Role of
1127 mTOR in autophagic and lysosomal reactions to environmental stressors in molluscs.
1128 *Aquatic Toxicol.*, 195, 114–128.

1129 Sforzini, S., Oliveri, C., Barranger, A., Jha, A.N., Banni, M., Moore, M.N., Viarengo, A., 2020.
1130 Effects of fullerene C₆₀ in blue mussels: role of mTOR in autophagy related
1131 cellular/tissue alterations. *Chemosphere*, DOI: 10.1016/j.chemosphere. 2019.125707

1132 Shannon, P., Markiel, A., Ozier, O., Baliga, N.S., Wang, J.T., Ramage, D., Amin, N.,
1133 Schwikowski, B., Ideker, T., 2003. Cytoscape: a software environment for integrated
1134 models of biomolecular interaction networks. *Genome Res.* 13, 2498-2504.

1135 Shaw, J.P., Dondero, F., Moore, M.N., Negri, A., Dagnino, A., Readman, J.W., Lowe, D.M.,
1136 Frickers, P.E., Beesley, A., Thain, J.E., Viarengo, A., 2011. Integration of biochemical,

1137 histochemical and toxicogenomic indices for the assessment of health status of mussels
1138 from the Tamar Estuary, U.K. Mar. Environ. Res., 72, 13-24.

1139 Shaw, J.P., Moore, M.N., Readman, J.W., Mou, Z., Langston, W.J., Lowe, D.M., Frickers, P.E.,
1140 Al-Moosawi, L., Pascoe, C., Beesley, A., 2019. Oxidative stress, lysosomal
1141 damage damage and dysfunctional autophagy in molluscan hepatopancreas (digestive
1142 gland) induced by chemical contaminants. Mar. Environ. Res., 152, 104825. doi.org/10.
1143 1016/j.marenvres.2019.104825.

1144 Stelling, J., Sauer, U., Szallasi, Z., Doyle, F.J., Doyle, J., 2004. Robustness of cellular
1145 functions. Cell, 118, 675-685.

1146 Stern, S.T., Adiseshaiah, P.P., Crist, R.M., 2012. Autophagy and lysosomal dysfunction as
1147 emerging mechanisms of nanomaterial toxicity. Particle and Fibre Toxicology, 9:20.
1148 <https://doi.org/10.1186/1743-8977-9-20>.

1149 Stone V., Donaldson, K., 2006. Nanotoxicology: signs of stress. Nature Nanotechnology, 1(1),
1150 23–24.

1151 Von Moos, N., Burkhardt-Holm, P., Köhler, A., 2012. Uptake and effects of microplastics on
1152 cells and tissue of the blue mussel *Mytilus edulis* L. after an experimental exposure.
1153 Environ. Science Technol., 46, 11327–11335.

1154 Wang, F., Gómes-Sintes, R., Boya, P., 2018. Lysosomal membrane permeabilization and cell
1155 death. Traffic, 19, 918-931.

1156 Ward, D. M., Leslie, J. D., & Kaplan, J., 1997. Homotypic lysosome fusion in macrophages:
1157 analysis using an in vitro assay. J. Cell Biol., 139(3), 665–673.

1158 Winston, G.W., Moore, M.N., Straatsburg, I., Kirchin, M., 1991. Lysosomal stability in *Mytilus*
1159 *edulis* L.: potential as a biomarker of oxidative stress related to environmental
1160 contamination. Arch. Environ. Contam. Toxicol., 21, 401-408.

1161 Yang, Y., Liu, X., Zhang, X.X., Korenaga, T., 2001. Study on the dynamic complexation
1162 between protein and PAHs by capillary electrophoresis. Analyt. Sciences, 2001
1163 17(ICAS2001): i1345-i1349.

1164 Yu, Z., Persson, H.L., Eaton, J.W., Brunk, U.T., 2003. Intralysosomal iron: a major determinant
1165 of oxidant-induced cell death. *Free Radical Biol. Med.*, 34(10), 1243-1252.
1166 doi:10.1016/s0891-5849(03)00109-6

1167 Zanger, R.C., Davydov, D., Venna, S., 2004. Mechanisms that regulate production of reactive
1168 oxygen species by cytochrome P450. *Toxicol. Appl. Pharmacol.*, 199, 316-31.

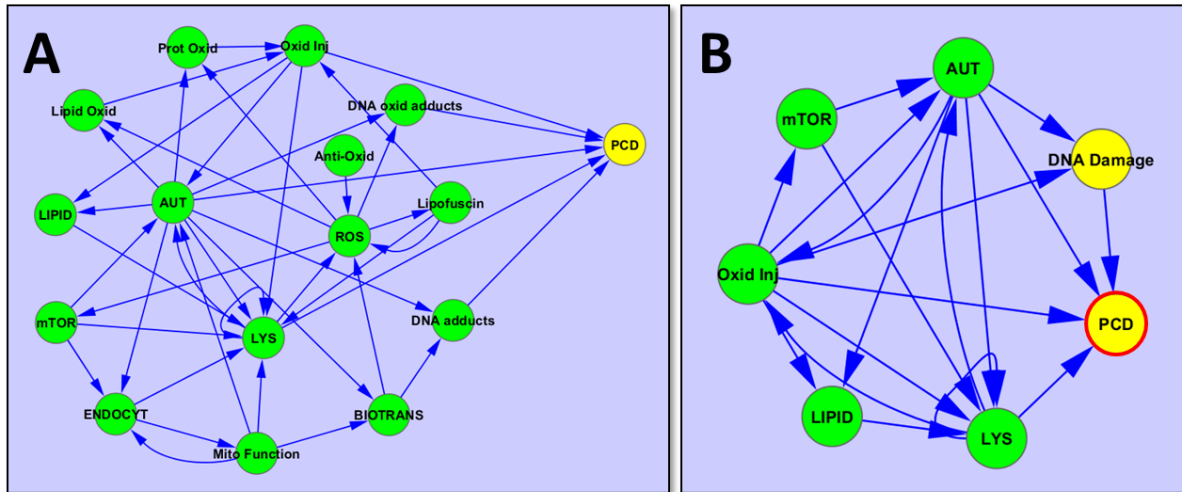
1169 Zhang, S., Zhang, J., Chen, H., Wang, A., Liu, Y., Hou, H., Hu, Q., 2019. Combined cytotoxicity
1170 of co-exposure to aldehyde mixtures on human bronchial epithelial BEAS-2B cells.
1171 *Environ. Pollut.*, 250, 250-261.

1172 Zhao, Y.G., Zhang, H., 2019. Autophagosome maturation: an epic journey from the ER to
1173 lysosomes. *J. Cell Biol.*, 218(3), 757-770.

1174 Zhao, Y., Hu, X., Liu, Y., Dong, S., Wen, Z., He, W., Zhang, S., Huang, Q., Shi, M., 2017. ROS
1175 signaling under metabolic stress: cross-talk between AMPK and AKT pathway.
1176 *Molecular Cancer* (2017) 16:79. DOI 10.1186/s12943-017-0648-1.

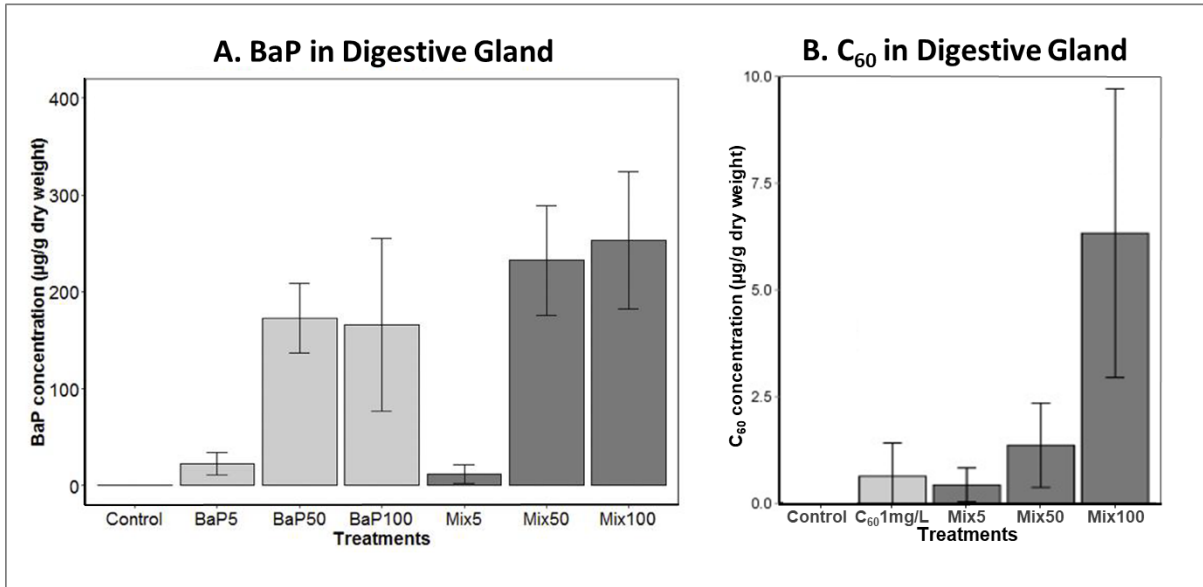
1177

1178



1179

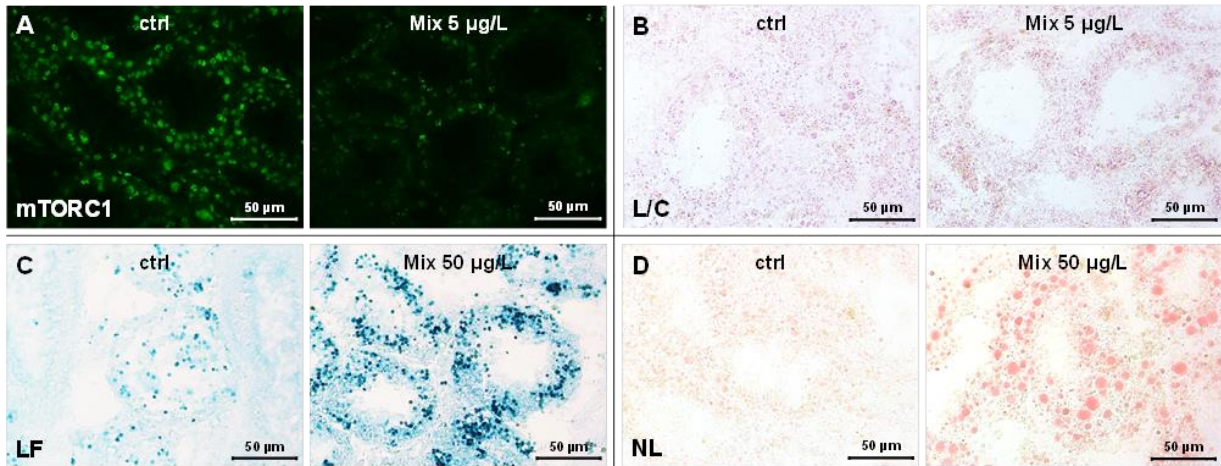
1180 Fig. 1. **A.** Interaction network model based on the physiological and pathological processes
 1181 represented by the biomarker investigations in mussel digestive cells. Processes
 1182 represented include endocytosis (cell feeding), lysosomal function (highly connected
 1183 hub), autophagy (highly connected hub), phosphorylated mTORC1 signalling, lysosomal
 1184 lipid accumulation, oxidative cell injury, DNA damage, cytochrome P450 mediated
 1185 biotransformation and Programmed Cell Death (PCD – yellow node:- apoptosis – type
 1186 1 PCD; autophagic – type 2 PCD; necrotic – type 3 PCD). **B.** Abbreviated network
 1187 corresponding to the biomarkers actually deployed in the current study. The calculation
 1188 of connectance % did not include values for yellow nodes DNA damage and PCD (red
 1189 outline). Green nodes represent those included in the determination of system
 1190 complexity (connectance - C_v %). AUT – autophagy, Anti-Oxid – anti-oxidative protection,
 1191 BIOTRANS – Cytochrome P450 (CYP) mediated biotransformation, ENDOCYT –
 1192 endocytosis, DNA adducts – organic xenobiotic derived adducts, DNA oxid adducts –
 1193 oxidative adducts, LIPID – lysosomal triglyceride (lipidosis), Lipid Oxid – lipid
 1194 peroxidation, Lipofuscin – ceroid lipofuscin (stress pigment), LYS – lysosomal function,
 1195 mTOR – mTORC1, Mito Function – mitochondrial energy metabolism, Oxid Inj –
 1196 oxidative cell injury, PCD – programmed cell death (apoptotic, autophagic and necrotic
 1197 cell death), Prot Oxid – protein oxidation (carbonyls); and ROS – reactive oxygen
 1198 species.



1199

1200 Fig. 2. C₆₀ and BaP concentrations in digestive gland tissue:- A. gas chromatography-mass
 1201 spectrometry (GC-MS) analyses of BaP in digestive gland (mean ± SE); B. liquid
 1202 chromatography-mass spectrometry (LC-MS) analyses of C₆₀ in digestive gland (mean
 1203 ± SE) with C₆₀ levels for Mix 100 treatment being significantly different from the controls
 1204 and other treatments ($P \leq 0.05$, $n = 3$, Tukey post-hoc test) . Data adapted from
 1205 Barranger et al. (2019a).

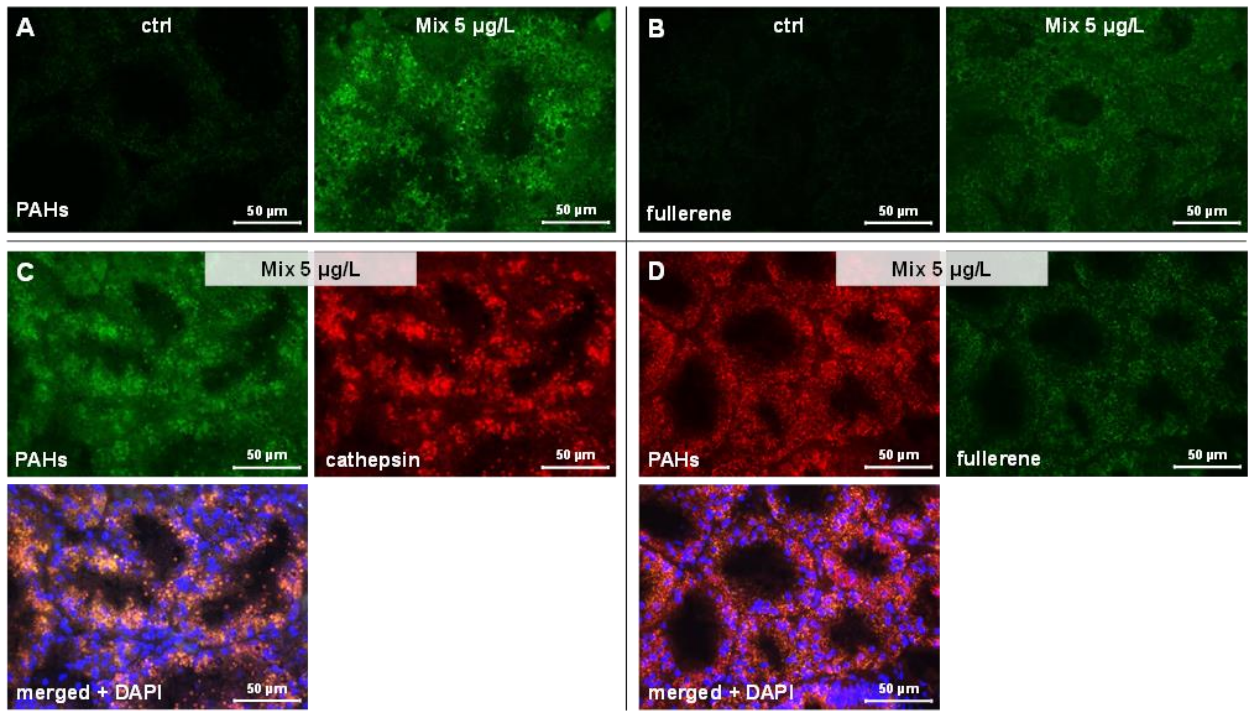
1206



1207

1208 Fig. 3. Representative paired images of the lysosomal and autophagy-related biomarker
 1209 changes in the digestive gland tissue sections from controls and exposed mussels: **A.**
 1210 anti-phosphorylated-mTORC1 immunocytochemical fluorescence reaction (green:
 1211 Chromeo conjugated secondary antibody); **B.** L/C volume ratio; **C.** lysosomal lipofuscin
 1212 (LF) accumulation (lipofuscinosis); and **D.** lysosomal lipid (NL) accumulation (lipidosis).

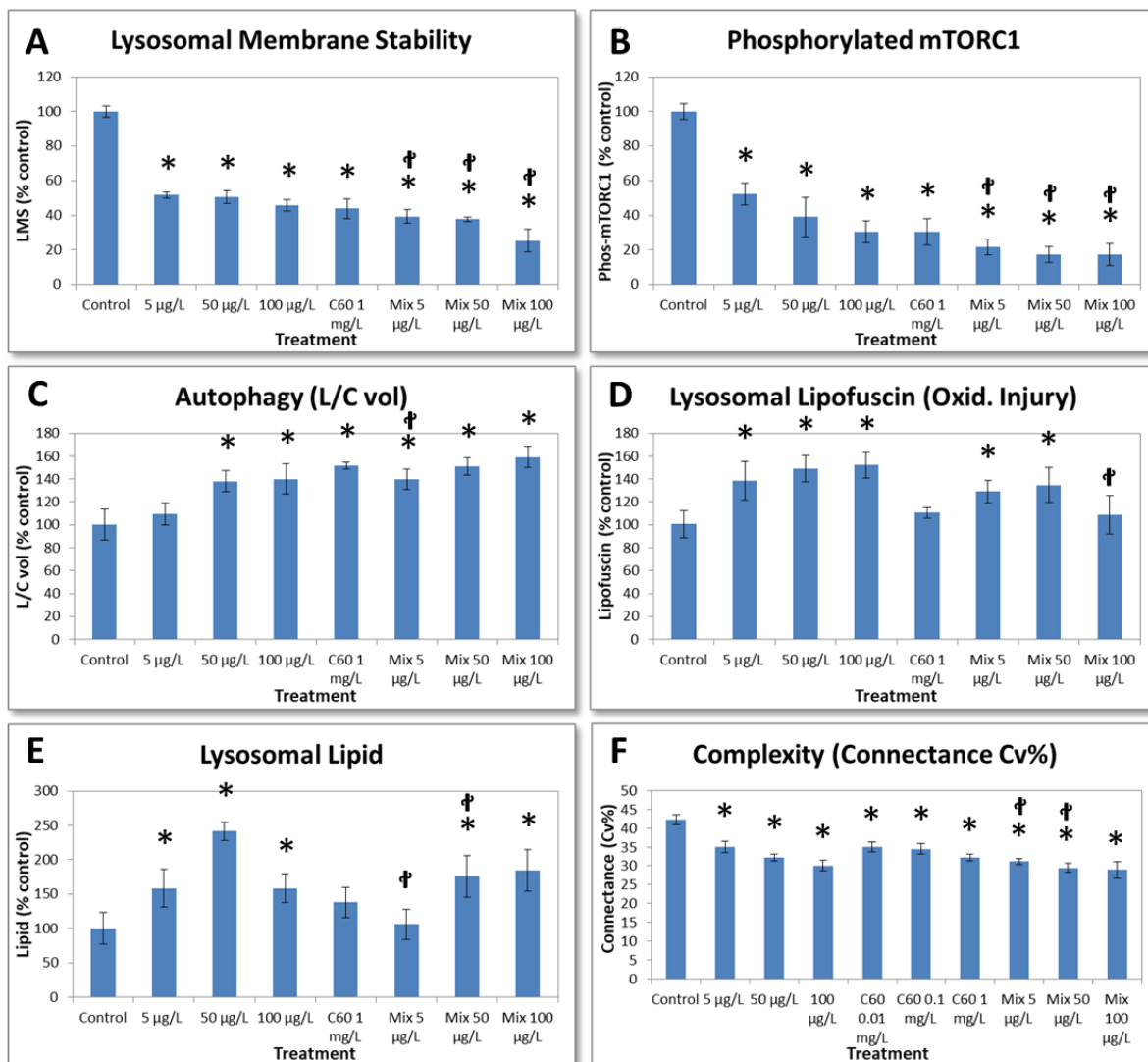
1213



1214

1215 Fig. 4. **A.** Anti-PAHs immunofluorescence for the detection of BaP; **B.** anti-fullerene
 1216 immunofluorescence (green: FITC conjugated secondary antibody) of digestive gland
 1217 tissue sections from control and Mix 5 µg/L treated animals; **C.** double
 1218 immunocytochemical fluorescent reactions in digestive cells from mussels treated with
 1219 Mix 5 µg/L reacted with anti-PAHs and anti-cathepsin D antibodies (separate colour
 1220 images for PAHs [FITC, green] and cathepsin D [DyLight 594, red]) - immunoreactivities
 1221 were merged into a composite image, whereby the co-localization of both antigens
 1222 resulted in a yellow colour; and **D.** double immunofluorescence of digestive cells from
 1223 animals treated with Mix 5 µg/L reacted with anti-PAHs and anti-fullerene antibodies
 1224 (separate colour images for PAHs [Alexa Fluor® 568, red] and fullerene [FITC, green] -
 1225 immunoreactivities were merged into a composite image, whereby the co-localization of
 1226 both antigens resulted in a yellow-orange colour. In the merged pictures, nuclei were
 1227 stained with DAPI (blue fluorescence).

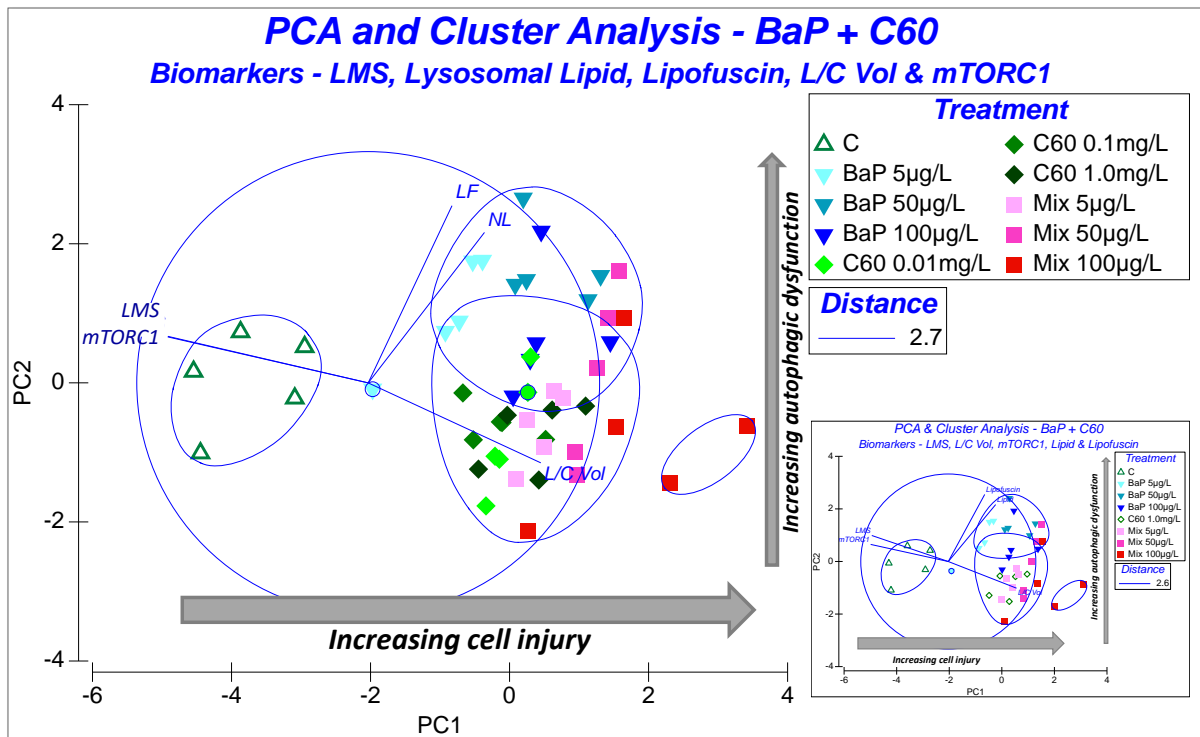
1228



1229

1230 Fig. 5. Biomarker data for the experimental treatments with C₆₀ fullerene (1 mg/L), BaP (5, 50
 1231 & 100 μ g/L) and mixtures of both compounds: **A.** Lysosomal membrane stability (LMS);
 1232 **B.** Lysosomal lipid (lipidosis); **C.** Autophagy measured as lysosomal volume / cell
 1233 volume (L/C vol ratio); **D.** Phosphorylated mTORC1; **E.** Lipofuscin (lipofuscinosis); and
 1234 **F.** Network complexity measured as connectance (C_v%) including 0.01 and 0.1 mg/L C₆₀
 1235 fullerene (biomarker data from Sforzini et al., 2020). All treatments were tested against
 1236 the control (* $P \leq 0.05$; Mann-Whitney U test and t-test); and the biomarker and
 1237 connectance values (mean \pm 95% CL/ $\sqrt{2}$, n = 5) are also significantly different ($P \leq 0.05$,
 1238 t-test) if the error bars do not overlap (Lowe et al., 1981; Buzatto et al., 2015); † $P \leq 0.05$
 1239 (t-test) for pairwise tests between BaP 5, 50 & 100 μ g/L and MIX 5, 50 & 100 μ g/L.

1240



1241

1242 Fig. 6. Principal component (PCA) and cluster analysis of the C₆₀ and BaP biomarker data

1243 biomarker data not including DNA damage, but including data for 0.01 and 0.1 mg/L C₆₀.

1244 Vectors indicate the directionality of specific biomarkers. **Arrows indicate:-** a.

1245 Increasing Cell Injury corresponding to the first principal component (PC1); and b.

1246 Increasing trend for Autophagic Dysfunction based on elevated intralysosomal lipofuscin

1247 and lipid, and corresponding to the second principal component (PC2). **Inset:-** PCA

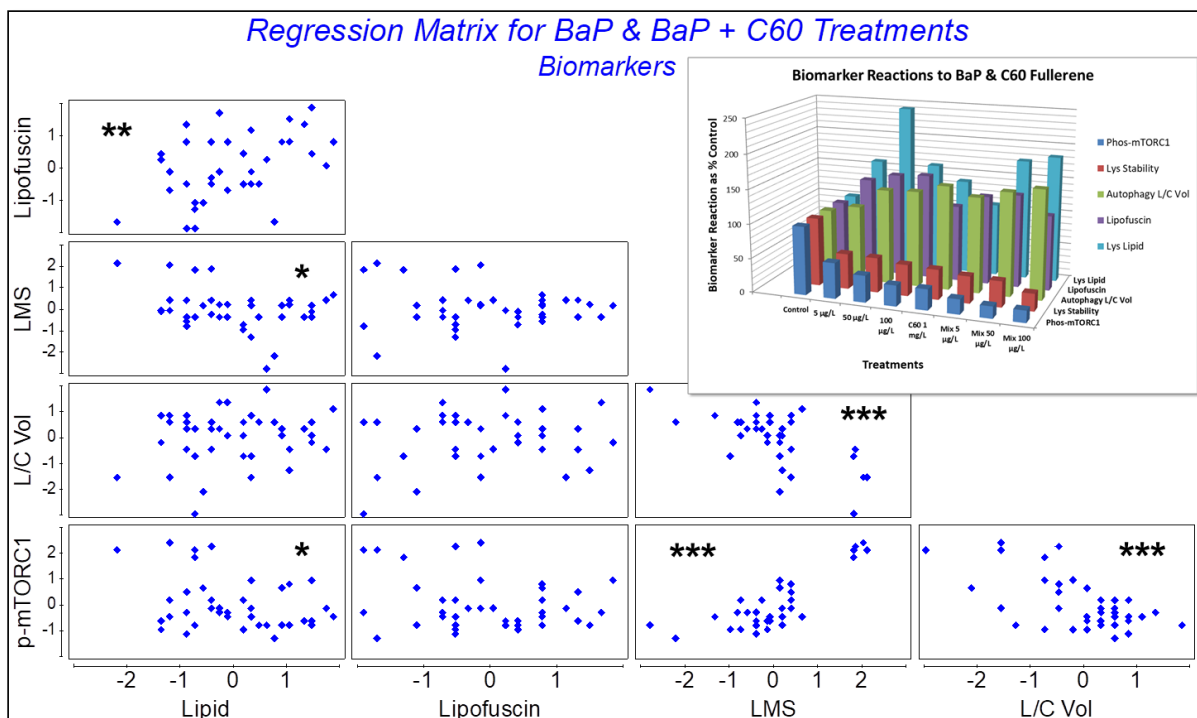
1248 excluding data for 0.01 and 0.1 mg/L C₆₀. **Vectors:-** LMS – lysosomal membrane

1249 stability; L/C Vol – lysosome/cell volume ratio (autophagy biomarker); LF – lysosomal

1250 lipofuscin (lipofuscinosis); NL – lysosomal lipid (lipidosis); and mTORC1 –

1251 phosphorylated mTORC1.

1252

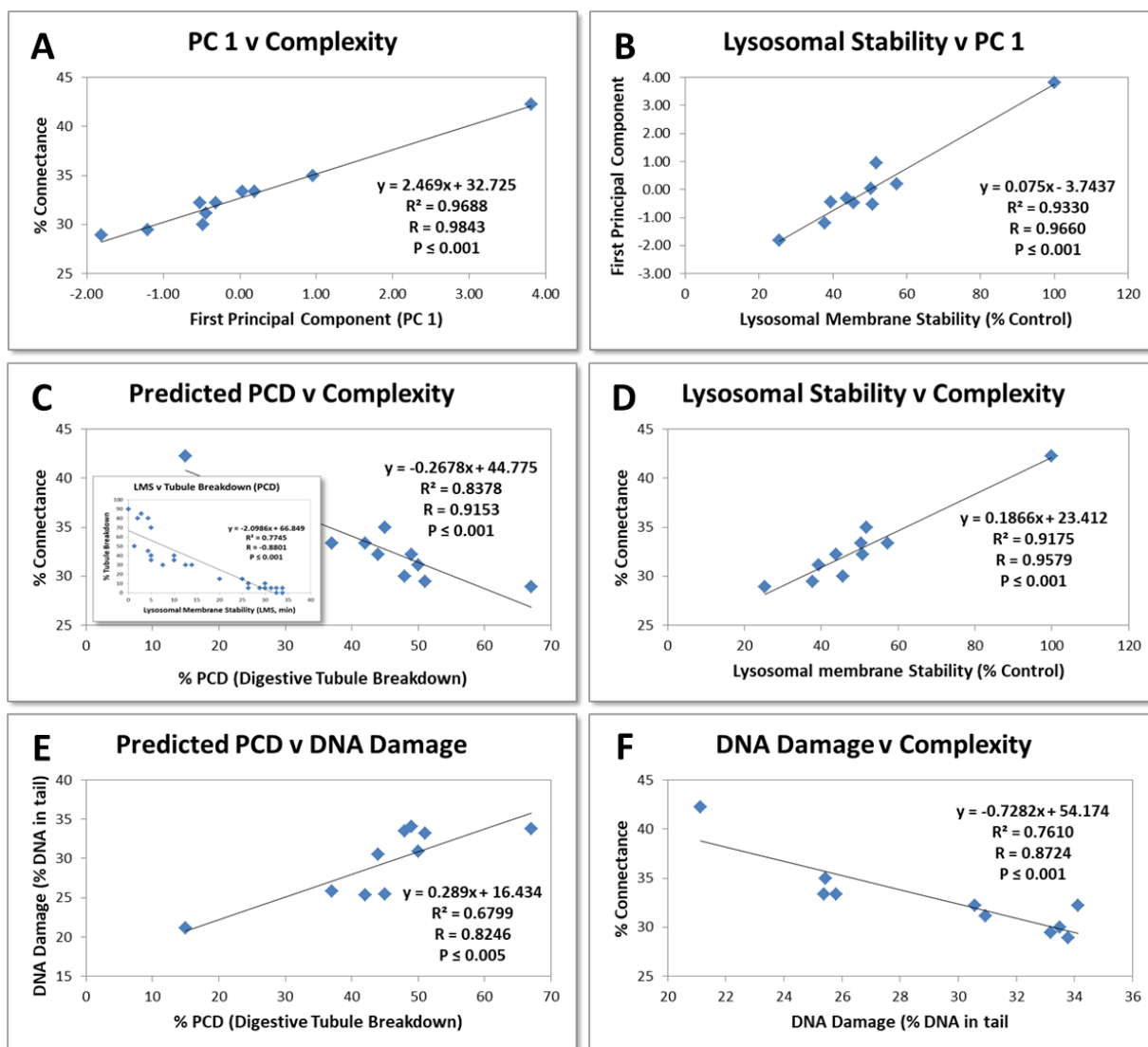


1253

1254 Fig. 7. Regression matrix for the C₆₀ and BaP biomarker data. **Inset:-** 3D summary plot of the

1255 biomarker reactions to the experimental treatments. Pearson's correlation coefficient: *

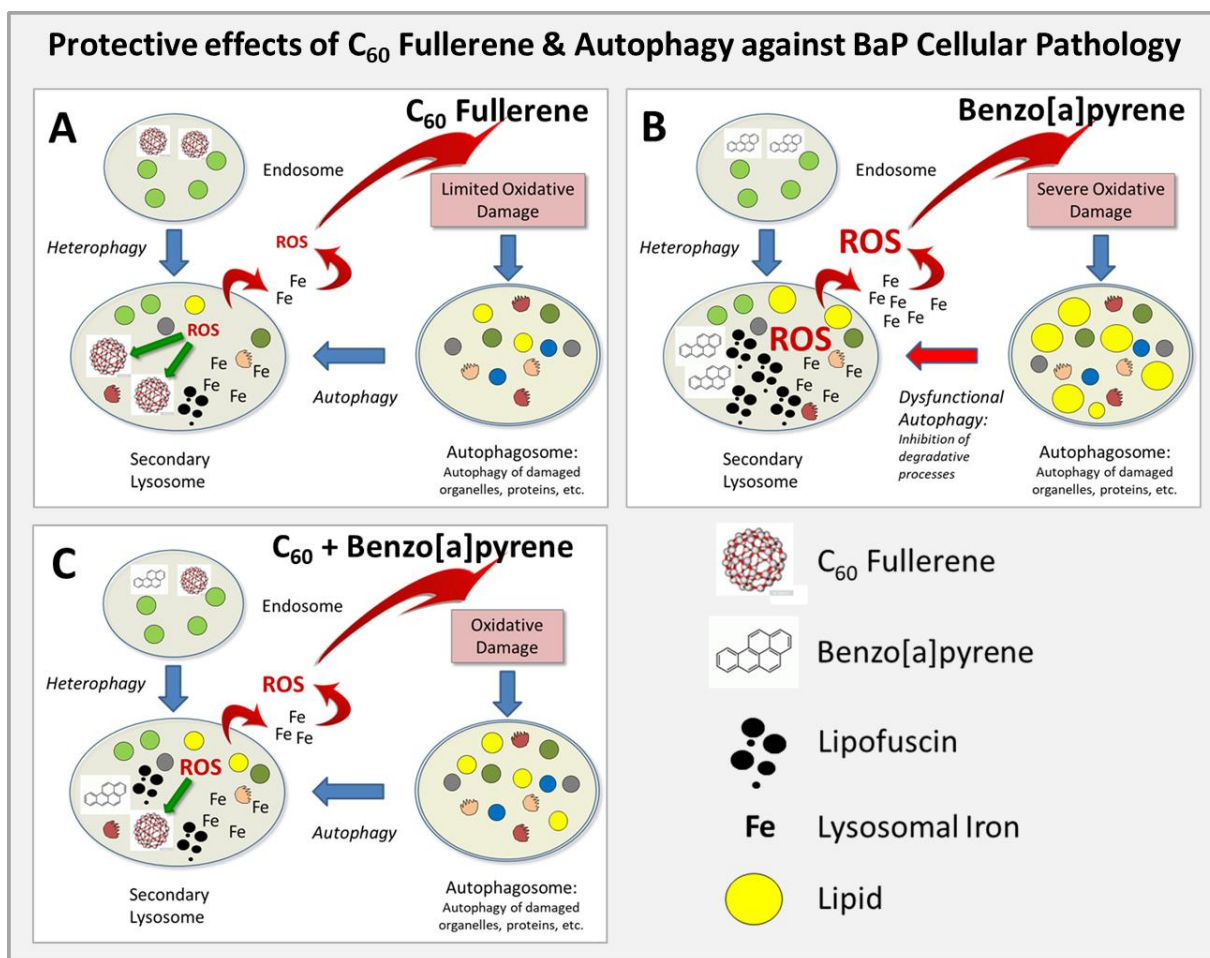
1256 indicates $P \leq 0.05$; ** indicates $P \leq 0.01$; *** indicates $P \leq 0.001$; n = 40.



1257

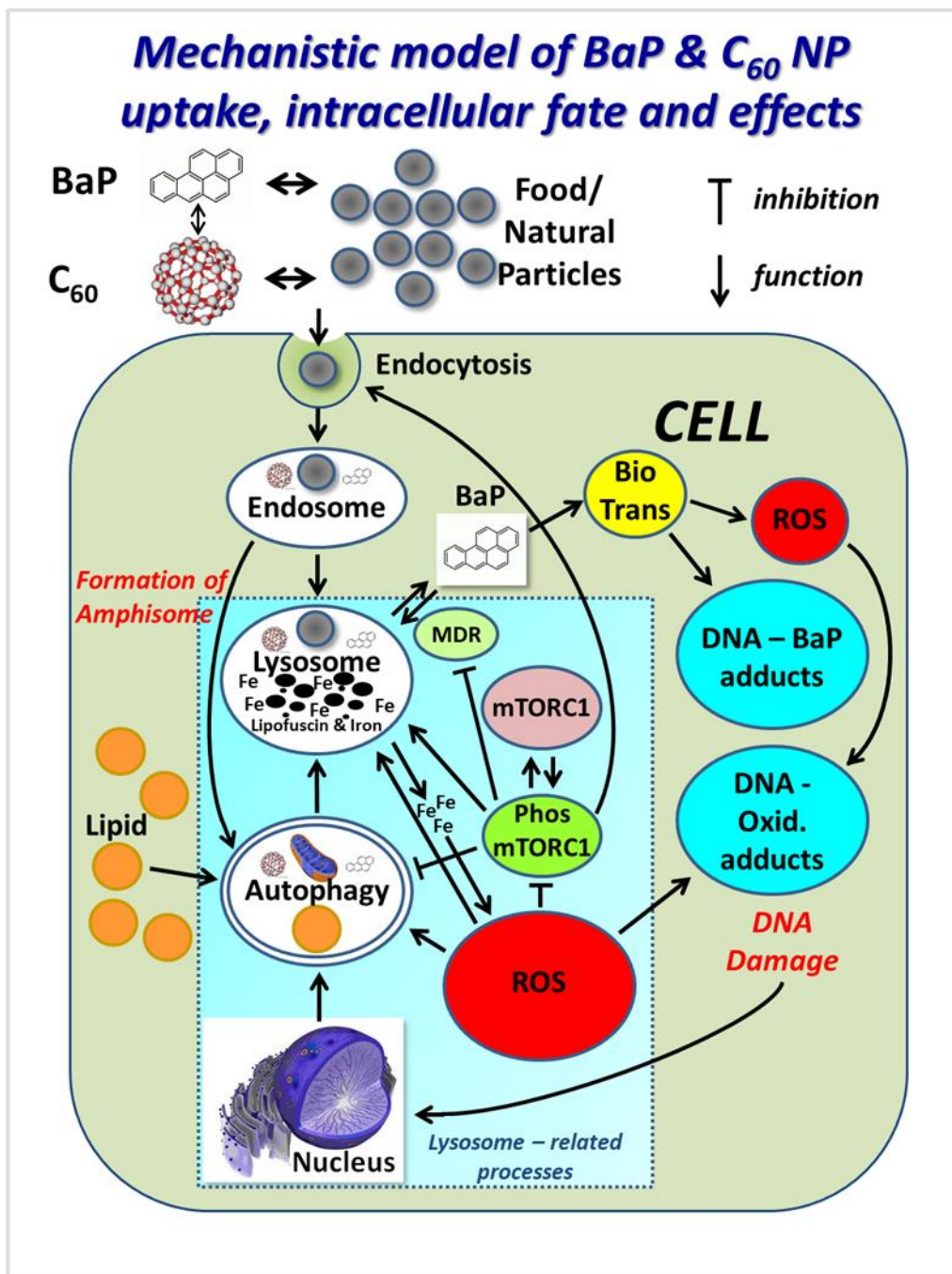
1258 Fig. 8. Statistical modelling of system complexity ($C_v\%$), lysosomal stability, predicted
 1259 programmed cell death and DNA damage based on C_{60} and BaP biomarker data
 1260 (including data for 0.01 and 0.1 mg/L C_{60}) versus: **A.** first principal component (PC 1) v
 1261 complexity; **B.** Lysosomal membrane stability (LMS) versus PC 1; DNA damage
 1262 (Comet); **C.** Predicted programmed cell death (PCD) v complexity (**Inset:** – LMS v
 1263 digestive tubule breakdown as indicator of PCD); **D.** lysosomal stability versus
 1264 complexity; and **E.** Predicted programmed cell death (PCD) versus DNA damage; and
 1265 **F.** DNA damage versus complexity. Coefficient of determination (R^2), Pearson's
 1266 correlation coefficient (R), and probability values (one-tailed test).

1267



1268

1269 Fig. 9. Subcellular reactions to:- **A.** C₆₀ fullerene; **B.** BaP; and **C.** C₆₀ + BaP. Conceptual model
 1270 deduced from the observed lysosomal cytoprotective effects of C₆₀ scavenging (green
 1271 arrows) of intra-lysosomal ROS (generated by iron and lipofuscin-bound iron) and
 1272 autophagic cytoprotection against BaP induced oxidative cell injury (i.e., autophagic
 1273 dysfunction, oxidative stress and including DNA damage). Intralysosomal iron is
 1274 released when lysosomal membrane stability is reduced by accumulation of C₆₀ and
 1275 BaP, as well as the injurious action of lysosomal hydrolases and ROS (i.e., increased
 1276 lysosomal membrane permeability; Kurz et al., 2008; Stern et al., 2012; Yu et al., 2003).
 1277 Increased autophagy of lipid results in lipidosis that tends to inhibit lysosomal
 1278 degradative processes contributing to autophagic and lysosomal dysfunction.



1279

1280 Fig. 10. Diagrammatic representation of an explanatory mechanistic framework for the
 1281 interconnected cellular reactions to C₆₀ and BaP based on the biomarker data, network
 1282 modelling and other published sources in the scientific literature (Sforzini et al., 2018).
 1283 Destabilisation of the lysosomal membrane (i.e., increased permeability) induced by
 1284 overload of BaP and C₆₀ will cause lysosomal hydrolase and iron (Fe) release into the
 1285 cytosol with resultant generation of reactive oxygen species (ROS) and degradation of

1286 macromolecules. Autophagy will have a cytoprotective effect by transporting oxidatively
1287 damaged proteins, damaged organelles (e.g., mitochondria) and damaged genomic
1288 components into the lysosomal compartment. Autophagosomes can also fuse with late
1289 endosomes to form amphisomes, which then mature into secondary lysosomes
1290 (Nakamura & Yoshimura, 2017). ROS will inhibit phosphorylated mTORC1 (active form),
1291 which will induce augmented autophagy (Brunk & Terman, 2002; Chen et al., 2010;
1292 Moore et al., 2006, 2015; Sforzini et al., 2018, 2019). Inhibition of mTORC1 will also
1293 inhibit endocytosis, further reduce lysosomal membrane stability and activate Pgp40
1294 (Boya, 2012; Flinn & Backer, 2010; Jiang & Liu, 2008). The increased flux of ROS will
1295 also contribute to fatty change (steatosis), with accumulation of autophagocytosed lipid
1296 within the lysosomal compartment resulting in lysosomal and autophagic dysfunction.
1297 Increased ROS flux will also cause oxidative damage to DNA (Canova et al., 1998); and
1298 enhanced autophagy may engulf portions of damaged and undamaged genomic
1299 material through partial nuclear autophagy (Buckland-Nicks & Hodgson, 2005; Mochida
1300 et al., 2015). Autophagy of nuclear DNA may contribute to autophagic and/or apoptotic
1301 programmed cell death as a pathological endpoint (Lowe, 1988; Lowe et al., 1981). ROS
1302 - reactive oxygen species; Phos mTOR - active phosphorylated form of mTORC1 cell
1303 signalling system; mTOR - inactive dephosphorylated form of mTORC1; MDR – Pgp40
1304 multidrug transporter; Biotrans Ph I & II - Phase I and II biotransformation system
1305 (Canova et al., 1998).

1306

1307 Table 1. Pearson's correlation coefficients for correlations between the first and second
 1308 principal components (PC1 & PC2) and individual biomarkers.

1309

<i>Principal Components</i>	<i>Lysosomal Lipid (Lipid)</i>	<i>Lipofuscin</i>	<i>Lysosomal Stability (LMS)</i>	<i>Lys/Cell Volume (L/C Vol)</i>	<i>mTORC1 (phosphorylated)</i>
PC1	-0.5413	-0.4160*	0.8739***	-0.7799***	0.8874***
PC2	0.6509***	0.7663***	0.2973	-0.3048	0.1955

1310 PC1 represents 52.5% of the variability, and PC2 24.6 % of the variability. * Indicates significance at
 1311 the 5% level, ** significance at the 1% level, and *** significance at the 0.1% level, two-tailed test; n =
 1312 40. Does not include the data for 0.01 and 0.1 mg/L C₆₀.

1313

1314 Table 2. Intracellular interactions (edges or links E) used in the network model* for the
 1315 determination of connectance (Cv %) as a measure of system complexity.

Interaction	Abbreviation	Biomarker
<i>Lysosomal function & Autophagy</i>	LYS-AUT	Lysosomal membrane stability (LMS)
<i>Lysosomal function & Oxidative injury</i>	LYS-Oxid Inj	Lysosomal membrane stability (LMS)
<i>Autophagy & Lysosomal function</i>	AUT-LYS	Lysosome/Cell volume ratio (L/C vol)
<i>Autophagy & Oxidative injury</i>	AUT-Oxid Inj	Lysosome/Cell volume ratio (L/C vol)
<i>Autophagy & DNA damage</i>	AUT-DNA damage	Lysosome/Cell volume ratio (L/C vol)
<i>Triglyceride lipid & Lysosomal function</i>	LIPID-LYS	Lysosomal lipid (triglyceride)
<i>Triglyceride lipid & Autophagy</i>	LIPID-AUT	Lysosomal lipid (triglyceride)
<i>Phosphorylated mTORC1 & Lysosomal function (permeability)</i>	mTOR-LYS	Phosphorylated mTORC1 kinase (phos-mTORC1)
<i>Phosphorylated mTORC1 & Autophagy</i>	mTOR-AUT	Phosphorylated mTORC1 kinase (phos-mTORC1)
<i>Oxidative cell injury & Autophagy</i>	Oxid Inj-AUT	Lysosomal Lipofuscin
<i>Oxidative cell injury & Lysosomal function</i>	Oxid Inj-LYS	Lysosomal Lipofuscin
<i>Oxidative cell injury & Lipid (fatty change)</i>	Oxid Inj-LIPID	Lysosomal Lipofuscin
<i>Oxidative cell injury & phosphorylated mTORC1</i>	Oxid Inj-mTOR	Lysosomal Lipofuscin
<i>Oxidative cell injury & DNA damage</i>	Oxid Inj-DNA damage	Lysosomal Lipofuscin

1316
 1317 * PCD node (vertex) was not included in the determination of complexity in the network (Fig. 1B).

1318

1319

1320 Table 3. Interaction Factors (IF) for the combined effects of C₆₀ fullerene and benzo[a]pyrene
 1321 (BaP) on the various biomarkers and connectance (C_v%).

Treatment Mixture	DNA Damage (COMET)	Lysosomal Stability (LMS)	mTORC1 (phos-mTORC1)	Lysosomal Lipid	Lysosomal Lipofuscin	Autophagy (Lysosomal/Cell Volume Ratio)	Network Complexity (Connectance – C _v %)
Mix C₆₀ 1mg/l + BaP 5μg/l	-7.48 ± 6.63 (0 ± 6.31)	-44.0* ± 8.7 (0 ± 7.72)	-39.1* ± 13.2 (0 ± 11.74)	-90.4* ± 47.5 (0 ± 42.1)	-21.81 ± 23.34 (0 ± 21.00)	-21.9 ± 21.5 (0 ± 18.9)	-6.12* ± 2.42 (0 ± 2.30)
Mix C₆₀ 1mg/l + BaP 50μg/l	-10.39† ± 6.42 (0 ± 5.97)	-43.2* ± 8.7 (0 ± 8.58)	-47.9* ± 16.6 (0 ± 15.65)	-104.25* ± 46.1 (0 ± 34.6)	-25.77 ± 16.99 (0 ± 16.99)	-39.0† ± 20.5 (0 ± 18.7)	-7.24* ± 2.37 (0 ± 2.05)
Mix C₆₀ 1mg/l + BaP 100μg/l	-12.69* ± 6.05 (0 ± 5.82)	-36.0* ± 11.0 (0 ± 8.28)	-56.6* ± 13.2 (0 ± 11.74)	-12.9 ± 48.4 (0 ± 37.7)	-54.71* ± 21.08 (0 ± 16.92)	-32.9† ± 19.5 (0 ± 16.6)	-8.89* ± 3.13 (0 ± 1.98)

1322
 1323 Interaction Factor ± 95% Confidence Limit /√2 (Buzatto et al., 2015). * indicates significance at the 5%
 1324 level, and † indicates significance at the 10% level. A negative IF indicates antagonism; an IF of 0
 1325 indicates additivity; and a positive IF indicates synergism. Statistical significance as indicated by * was
 1326 determined by testing for overlap between the mixture IF ± 95% CL/√2 and the predicted additive value
 1327 for C₆₀ and BaP, assumed to have an IF = 0 ± 95% CL/√2, where the confidence limit is derived from
 1328 the SEM_(add) value for the additive C₆₀ and BaP. DNA damage data was incorporated from Barranger et
 1329 al. (2019a). Additive values (IF = 0 ± 95% CL/√2) are shown in parentheses for each treatment and
 1330 biomarker.

1331
 1332
 1333